Engineered Three-Dimensional Tumor Models to Study Natural Killer Cell Suppression

Madison N. Temples[1], Isaac M. Adjei[1], Phoebe M. Nimocks[1], Julie Djeu[2], and Blanka Sharma[1]*

Author Addresses:

[1]J. Crayton Pruitt Department of Biomedical Engineering, University of Florida

1275 Center Drive Biomedical Sciences Building JG-56

P.O. Box 116131

Gainesville, Florida 32611-6131

[2]Department of Immunology, Moffitt Cancer Center

12902 Magnolia Drive MRC 4E

Tampa, Florida 33612-9497

*Blanka Sharma, Ph.D. (Corresponding author)

J. Crayton Pruitt Department of Biomedical Engineering, University of Florida

1275 Center Drive Biomedical Sciences Building JG-56

P.O. Box 116131

Gainesville, Florida 32611-6131

blanka.sharma@bme.ufl.edu

Phone: (352) 273- 9329

Fax: (352) 273 - 9221

Key Words: Natural Killer Cells, Tumor Models, PEG hydrogel, Immunosuppression, Migration

Abstract:

A critical hurdle associated with natural killer (NK) cell immunotherapies is inadequate infiltration and function in the solid tumor microenvironment. Well-controlled 3D culture systems could advance our understanding of the role of various biophysical and biochemical cues that impact NK cell migration in solid tumors. The objectives of this study were to establish a biomaterial which (i) supports NK cell migration and (ii) recapitulates features of the *in vivo* solid tumor microenvironment, to study NK infiltration and function in a 3D system. Using peptide functionalized poly(ethylene glycol)-based hydrogels, the extent of NK-92 cell migration was observed to be largely dependent on the density of integrin binding sites and the presence of matrix metalloproteinase degradable sites. When lung cancer cells were encapsulated into the hydrogels to create tumor microenvironments, the extent of NK-92 cell migration and functional activity was dependent on the cancer cell type and duration of 3D culture. NK-92 cells showed greater migration into the models consisting of non-metastatic A549 cells relative to metastatic H1299 cells, and reduced migration in both models when cancer cells were cultured for 7 days versus 1 day. In addition, the production of NK-cell related pro-inflammatory cytokines and chemokines was reduced in H1299 models relative to A549 models. These differences in NK-92 cell migration and cytokine/chemokine production corresponded to differences in the production of various immunomodulatory molecules by the different cancer cells, namely the H1299 models showed increased stress ligand shedding and immunosuppressive cytokine production, particularly TGF-β. Indeed, inhibition of TGF-β receptor I in NK-92 cells restored their infiltration in H1299 models to levels similar to that in A549 models, and increased overall

infiltration in both models. Relative to conventional 2D co-cultures, NK-92 cell mediated cytotoxicity was reduced in the 3D tumor models, suggesting the hydrogel serves to mimic some features of the biophysical barriers in *in vivo* tumor microenvironments. This study demonstrates the feasibility of a synthetic hydrogel system for investigating the biophysical and biochemical cues impacting NK cell infiltration and NK cell-cancer cell interactions in the solid tumor microenvironment.

Introduction

Natural killer (NK) cells are emerging as a powerful tool for immunotherapies because they exert potent cytotoxic effects on cancer cells without the need for priming or knowledge of specific tumor antigens. Unlike T-cells, NK cells can employ cytotoxic function in an antigen independent manner, by utilizing receptors to recognize alterations in cell surface ligands on nascent tumor cells.[1,2] Natural killer cells exert their effector functions primarily through the perforin-granzyme pathway, death receptor pathways, and cytokine release, while also triggering the activation of the adaptive immune system.[1,2] Accordingly, NK cells play a critical role in the surveillance of malignancies, as NK cell function has been negatively correlated with cancer occurrence and outcome,[3,4] and increased NK cell tumor infiltration is correlated with a better prognosis in various cancers.[5,6]

In clinical trials, adoptive transfer of NK cells to treat certain hematological malignancies has been safe, well tolerated by patients, and successful in inducing remission or halting tumor progression in a subset of patients.[7–9] However, NK cell therapy for the treatment of solid malignancies, which constitute the vast majority of cancer cases,[10] has proven more challenging.[11,12] Solid tumors pose both a physical barrier and a biochemical milieu that is highly immunosuppressive, resulting in inefficient NK cell infiltration[13–16] as well as impeding the NK

cell-cancer cell contact, required for their cytotoxic function.[17–20] The NK cells that are successful in migrating into the tumor are functionally inhibited by many soluble, insoluble, and membrane-bound immunosuppressive factors.[2,15,21,22] To evade NK cell recognition, the resulting combination of signals cancer cells deliver to an array of activating and inhibiting receptors on NK cells must be inhibitory. Thus, cancer cells upregulate inhibitory signals delivered to NK cells, through major histocompatibility complex class I (human leukocyte antigens (HLA)) molecules, and downregulate and/or shed stress-induced cell surface ligands, like HLA-A, HLA-C, MICA/B and ULBP1/2, which relay activating signals to NK cells.[2] Suppressive soluble molecules derived from cancer and stromal cells, such as transforming growth factor β (TGF-β) and interleukin 6 (IL-6), further inhibit the cytotoxic potential of NK cells and their ability to produce cytokines, chemokines, and growth factors.[14,22,23] While the effects of various tumor-related immunosuppressive factors on NK cell-mediated cytotoxicity and cytokine and chemokine production have been well characterized, their influence on NK cell migration is not fully understood. Experimental NK cell immunotherapies have largely focused on enhancing the activating signals at the immune cell-cancer cell synapse;[17,21] however, understanding and enhancing the vital step of NK cell migration into solid tumors are critical for the development of effective therapies.

Given that NK cells must migrate through the three-dimensional (3D) tumor matrix to establish contact with cancer cells, studying NK cell-cancer cell interactions in a 3D environment is imperative. Two-dimensional (2D) monolayer culture systems for analysis of NK cell-cancer cell interactions do not account for the complex 3D tumor microenvironment, and poorly correlate with *in vivo* and clinical outcomes.[24–26] While human tumor xenograft models in mice provide insight into NK cell homing and cytotoxicity,[27,28] the complexity of studying immune

cell-cancer cell interactions *in vivo* limits mechanistic understanding of NK cell migration and its' inhibition. Additionally, human tumor xenografts studies have demonstrated limited NK cell infiltration, especially after intravenous injection,[29,30] requiring investigators to genetically engineer cancer cells to express chemokines, like CXCL10, to increase NK cell infiltration into the tumor.[31] Matrigel and spheroid culture systems, which are commonly used in cancer biology, have been employed to study NK cell-cancer cell interactions in 3D.[32–37] However, these systems do not allow for control of the extracellular biochemical or biophysical cues, limiting the ability to delineate which parameters of the 3D system influence NK cell migration. Furthermore, not all cancer cell lines readily form tumor spheroids. To overcome these limitations, hydrogels derived from synthetic polymers have been employed to study tumor biology, which enable precise control over cell source, material components, and mechanical and biochemical cues.[38–40] Specifically, polyethylene glycol (PEG)-based hydrogels have been useful in interrogating the effects of 3D mechanical and biochemical properties on cancer cell growth and migration,[26] epithelial to mesenchymal transition,[25,39] and angiogenesis.[41] This study builds on the knowledge from previous model systems and leverages the tunable properties of PEG-based hydrogels to study NK cell migration and NK cell-cancer cell interactions for the first time.

The long-term goal of this research is to develop biomimetic models of the tumor microenvironment to uncover mechanisms of NK cell infiltration and activation in solid tumors. Working towards this goal, the objectives of the following study were to establish a hydrogel system that (I) supports NK cell migration and (II) recapitulates features of the tumor microenvironment to study NK cell infiltration and NK cell-cancer cell interactions in a 3D system. Since NK cells utilize matrix metalloproteinases (MMPs) [36,37,42,43] and integrins, such as $\alpha_v\beta_3$,[44] $\alpha_4\beta_7$,[45] and β_2 integrins,[46] in 2D and transwell chamber studies, the PEG-based hydrogels

were engineered to examine the effects of integrin binding and MMP expression on NK cell migration in 3D. To study NK cell-cancer cell interactions, we selected two different lung cancer cell lines that display distinct metastatic phenotypes and thus likely different profiles of immunomodulatory molecules. We hypothesized that the hydrogels would support the migration of NK cells, and the different biochemical cues in the *in vitro* tumor microenvironments would have distinct and measurable effects on the NK cell response.

Experimental Details

Materials:

Calcein acetoxymethyl (AM), Invitrogen™ Molecular Probes™ LIVE/DEAD™ Viability/Cytotoxicity kit, Quant-iT™ PicoGreen™ dsDNA assay kit, Hoescht 33258 dye, ELISA for stromal cell-derived factor 1 alpha (SDF-1α, for comparison of 2D to 3D cultures), and 1,1'-Dioctadecyl-3,3,3',3'-Tetramethylindocarbocyanine Perchlorate (DiI) stain were purchased from Invitrogen (Carlsbad, CA, USA). Human recombinant interleukin 2 (IL-2), SDF-1α, and transforming growth factor beta 1 (TGF-β1) were purchased from Peprotech (Rocky Hill, NJ, USA). Polyethylene glycol (PEG)-diacrylate (DA) (PEG-DA) molecular weights of 3.4 kDa and 10 kDa, and acrylate-PEG-succinimidyl valerate ester (SVA) (acryl-PEG-SVA) (MW 3.4 kDa) were purchased from Laysan Bio Inc. (Arab, AL, USA). The matrix metalloproteinase (MMP) degradable sequence, GGVPMS↓MRGGK, (MW 1076.31 Da) was purchased from Biomatik (Ontario, Canada). Cyclo(Arg-Gly-Asp-D-Phe-Lys) (RGD, MW 603.68 Da) and cyclo(Arg-Ala-Asp-D-Phe-Lys) (RAD, MW 617.71 Da) were purchased from Peptides International (Louisville, KY, USA). The dialysis tubing, Spectra/Por 6 2000 MWCO, was purchased from Spectrum Labs (Rancho Dominguez, California, USA). 2-Hydroxy-4'-(2-hydroxyethoxy)-2-methylpropiophenone (Irgacure 2959), paraformaldehyde, Triton X-100, the

broad range MMP inhibitor GM6001, and donkey and goat serum were purchased from Millipore Sigma (St. Louis, MO, USA). Reporter Lysis Buffer, CellTiter 96 ® AQ_{ueous} One Solution Cell Proliferation Assay (MTS assay), and CytoTox-ONE™ Homogeneous Membrane Integrity Assay were purchased from Promega (Madison, WI, USA). All ELISAs were purchased from Qiagen (Hilden, Germany), except for MICA, SDF-1α, and chemokine (C-X3-C) ligand 1 (CX3CL1) which were purchased from Millipore Sigma (St. Louis, MO, USA). The mouse anti-human antibody for MICA/B and the donkey anti-rabbit and goat anti-mouse FITC-tagged secondary antibodies were purchased from Santa Cruz Biotechnology (Dallas, TX, USA). Rabbit anti-human antibody for ULPB1 was purchased from Proteintech Group (Rosemont, IL, USA). The small molecule inhibitor of the TGF-β receptor type I kinase (TGFβRI), LY2157299, was purchased from Cayman Chemical (Ann Arbor, MI, USA). All other reagents were purchased from ThermoFisher Scientific Inc. (Waltham, MA, USA).

Cell Culture:

The metastatic, H1299 and non-metastatic, A549 human-derived non-small cell lung cancer (NSCLC) cell lines and the human-derived natural killer cell line, NK-92, were purchased from American Type Culture Collection (Manassas, VA, USA). The A549 and H1299 cells were cultured in RPMI 1640 without L-glutamine, supplemented with 10% (v/v) heat-inactivated fetal bovine serum (FBS), 1% (v/v) penicillin-streptomycin, and 1% (v/v) L-glutamine. The NK-92 cells were cultured in RPMI 1640 without L-glutamine, supplemented with 20% (v/v) heat-inactivated FBS, 1% (v/v) of penicillin-streptomycin, 1% (v/v) L-glutamine, 1% (v/v) minimum essential medium (MEM) non-essential amino acids (NEAA) solution, and 1% (v/v) sodium pyruvate. All NK-92 cell media was supplemented with 100 units/mL of IL-2. Cells were maintained at 37°C and 5% CO_2. The NK-92 cell line was utilized because it has been shown to

have the same functional and phenotypic characteristics as primary activated NK cells,[47] and has exceptional cytotoxicity against a broad range of primary and established tumor cells *in vitro* and *in vivo*.[47,48]

Peptide Functionalization and Polymer Synthesis:

To make the hydrogels sensitive to cell-mediated degradation, the MMP-sensitive peptide sequence VPMS↓MRGG was included. This peptide domain is sensitive to cleavage by numerous MMPs, including collagenase-1 (MMP-1), gelatinase A (MMP-2), and gelatinase B (MMP-9).[49] The peptide was modified to allow it to be capped on either end by a PEG acrylate group upon conjugation, as previously described.[49–52] Briefly, the sequence was modified with additional glycine (G) spacers and a c-terminal lysine (K), the final sequence being GGVPMS↓MRGGK. The MMP degradable block linked PEG, acryl-PEG-dMMP-PEG-acryl (MW ~7900 Da, PEG-dMMP-PEG), with the MMP-sensitive peptide GGVPMS↓MRGGK, was synthesized as previously described.[49–52] Briefly, the terminal and lysine amine groups of the MMP degradable sequence were reacted with the SVA of an acryl-PEG-SVA in 50 mM sodium bicarbonate (pH 8) at a 1:2 mole ratio for 4 hours. The reaction mixture was dialyzed for 24 hours against water to remove unreacted reagents, lyophilized for 48 hours, and stored at -20°C until use.

Cell adhesion was supported by the immobilization of a cell adhesion ligand to the crosslinked network. Arginine-glycine-aspartic acid (RGD) functionalized PEG, acryl-PEG-RGD (MW ~4000 Da, PEG-RGD), was synthesized as previously described.[50–52] Briefly, the terminal amine of cyclo(Arg-Gly-Asp-D-Phe-Lys)[51] (cRGD) reacted with acryl-PEG-SVA in 50 mM sodium bicarbonate (pH 8) at a 1.05:1 mole ratio for 4 hours. The reaction mixture was dialyzed for 24 hours against water to remove unreacted reagents, lyophilized for 48 hours, and

stored at -20°C until use. The specific cyclic RGD sequence that was incorporated into the hydrogels in this study mimics the adhesion site on vitronectin, which interacts with $\alpha_v\beta_3$ and $\alpha_v\beta_5$ integrins.[53–55] Acryl-PEG-RAD (MW ~4000 Da, PEG-RAD), a control with no integrin binding site, was synthesized in the same manner, by reacting the terminal amine of cyclo(Arg-Ala-Asp-D-Phe-Lys) with the SVA of an acryl-PEG-SVA.

Characterization of Hydrogel Mechanical Properties and Swelling Ratio:

The precursor solutions for different hydrogel formulations, made in PBS, with varying amounts of MMP degradable and RGD adhesion sites are listed in Table 1. 0.05% (w/v) of the photoinitiator, Irgacure 2959, was added to each precursor solution prior to polymerization. For control hydrogels without MMP degradable sites, the PEG-dMMP-PEG was substituted with non-degradable PEG-DA (10kDA) of comparable molecular weight. For mechanical testing, hydrogels were formed in cylindrical silicon molds (Grace Biolabs) 8 mm diameter by 1.7 mm depth. The precursor solution (108 μL) was added to the silicon mold and photopolymerized by OmniCure S1000 light (Excelitas Technologies, Corp., Waltham, MA, USA) for 4 minutes using 4.0 mW/cm^2 long wave ultraviolet A (UVA) light. After polymerization, the hydrogels were removed from the mold, rinsed in PBS, and incubated in PBS at 37°C and 5% CO_2 for 24 hours. The viscoelastic properties were examined using an Anton Paar MCR 302 rheometer (Graz, Austria) with parallel plate geometry according to established methods.[56,57] An 8 mm sandblasted top load cell was used to decrease slipping during testing. For approximation of physiological conditions, the Peltier plate was pre-heated to 37°C, and the samples were enclosed in a humidity chamber. For each hydrogel composition, amplitude sweeps from 0.01% to 100% strain were first conducted at 1 Hz to determine the linear viscoelastic range (LVE). The storage (*G'*) and loss (*G"*) moduli were then determined from frequency sweeps from 0.1 to 100

Hz at a strain value in the middle of the LVE, chosen as 0.1% strain for all hydrogel compositions. For all hydrogel compositions, shear moduli (G*) were determined from Equation (1) at 1 Hz and used to calculate Young's moduli (E) using Equation (2), and a Poisson's ratio (υ) of 0.5.[58–63] For each hydrogel composition, 3 samples were used for the amplitude sweeps and 4 hydrogels were used for the frequency sweeps, wherein each hydrogel was used only for 1 test.

$$G^* = \sqrt{G'^2 + G''^2} \quad (1)$$

$$E = 2G^*(1 + \upsilon) \quad (2)$$

To determine the swelling ratio, hydrogels of each composition (Table 1) were photopolymerized from 10 µL of precursor solution, as previously described. After polymerization, the gels were rinsed in PBS and added to wells containing PBS for 24 hours at 37°C and 5% CO_2. The hydrogels were then removed, carefully blotted to remove excess surface liquid, and the total swollen weight (W_s) was measured. Hydrogels were lyophilized for 24 hours, and total dry weight (W_d) was measured. The swelling ratio was calculated by Equation (3).

$$Swelling\ ratio = \frac{W_s - W_d}{W_d} \quad (3)$$

Table 1. Precursor solutions for hydrogels for NK-92 cell migration

Group	Precursor Solution Composition
1	50:50 ratio of 10% (w/v) PEG-DA (3.4 kDa) and 10% (w/v) PEG-dMMP-PEG, and 2 mM PEG-RGD
2	50:50 ratio of 10% (w/v) PEG-DA (3.4 kDa) and 10% (w/v) PEG-dMMP-PEG, and 5 mM PEG-RGD
3	50:50 ratio of 10% (w/v) PEG-DA (3.4 kDa) and 10% (w/v) PEG-dMMP-PEG, and 10 mM PEG-RGD
4	50:50 ratio of 10% (w/v) PEG-DA (3.4 kDa) and 10% (w/v) PEG-dMMP-PEG, and 5 mM PEG-RAD
5	50:50 ratio of 10% (w/v) PEG-DA (3.4 kDa) and 10% (w/v) PEG-DA (10kDa), and 5 mM PEG-RGD
6	50:50 ratio of 10% (w/v) PEG-DA (3.4 kDa) and 10% (w/v) PEG-DA (10kDa), and 5 mM PEG-RAD

Encapsulation of a Point Source into Hydrogels:

The different hydrogel compositions (Table 1) were constructed with an SDF-1α fibrin clot point source to assess NK-92 cell migration. Scheme S1 demonstrates the experimental set

up to make the hydrogels with the SDF-1α fibrin clot point source; first, 25 μL of precursor solution was added to a mold and photopolymerized by UVA light for 4 minutes, as previously described. To make the fibrin clot containing SDF-1α on top of the casted hydrogel, 2 μg/μL fibrinogen and 100 ng of SDF-1α totaling 3 μL was pipetted onto the gel, then 40 units of thrombin was added to the fibrinogen mixture and rested until a clot formed. Then, 25 μL of the same precursor solution was added on top of the casted gel/fibrin clot and exposed to the UV light for 4 minutes. The hydrogels were removed from the mold and rinsed in PBS. The hydrogels had an average diameter of 5.1 ± 0.09 mm. To determine the amount of SDF-1α released into the media by hydrogels with the fibrin clot point source, the hydrogels were incubated in NK-92 cell media, which was collected daily and SDF-1α was quantified via an ELISA, per manufacturers' instructions.

To further assess NK-92 cell migration, group 2 hydrogels (Table 1) were utilized to study the effects of TGF-β on NK-92 cell migration compared to SDF-1α. In these studies, the point source was an internal PEG-DA gel rather than a fibrin clot, to eliminate any confounding effects of protein binding to the fibrin. To generate point source gels, 10 μL of 10% PEG-DA in PBS containing 100 ng of SDF-1α, 100 ng of SDF-1α and 100ng of TGF-β1, or 100ng of TGF-β1 was photopolymerized as previously described. Then 25 μL of the group 2 precursor solution was added to the same mold as mentioned previously and photopolymerized as previously described. After polymerization, the 10 μL PEG-DA point source with encapsulated protein was centered on top of the 25 μL polymerized degradable PEG hydrogel in the mold, and 25 μL of the precursor solution was added to the mold and photopolymerized. The hydrogels were removed from the mold and rinsed in PBS.

Evaluation of NK-92 Cell Migration into Hydrogels:

Supplementary Scheme 1 shows the experimental set-up for NK-92 cell migration into the different hydrogel compositions with the SDF-1α point source (fibrin clot). The same experimental set-up was used for evaluating NK-92 cell migration towards SDF-1α, SDF-1α and TGF-β1, or TGF-β1, once the hydrogels were formed. Briefly, directly following crosslinking of the hydrogels and rinsing in PBS, NK-92 cell media containing 50,000 NK-92 cells was added to each well containing a hydrogel and placed on a mini shaker (VWR, Radnor, PA, USA) at 50 rpm in the incubator, to keep the cells from settling to the bottom of the wells. For the studies of NK-92 cell migration into different hydrogel compositions, with the SDF-1α fibrin clot point source, 4 mM calcein AM was added to each well at the end of 7 days of incubation, to stain the cells that migrated into the hydrogel. One hour after the addition of calcein AM, the hydrogels were rinsed in PBS and imaged with confocal microscopy. For studies of the effect of TGF-β1 on NK-92 cell migration (PEG-DA point source), NK-92 cells were incubated with the hydrogels for 7 days using the same conditions described previously. After which hydrogels were rinsed in PBS, fixed with 4% paraformaldehyde, stained with Hoescht 33258 dye for 4 hours, and imaged with confocal microscopy. Migration distance, measured as the distance from the edge of the hydrogel to the migrated NK-92 cells, and relative fluorescence values of NK-92 cells in the gels were determined using Fiji.[64]

To evaluate the mechanisms of NK-92 cell migration into the hydrogels, MMP inhibitor and integrin binding to soluble RGD studies were performed. For both studies the group 2 (Table 1) precursor solution was polymerized with an SDF-1α fibrin clot point source, as described previously. For the MMP inhibitor study, the same experimental set-up as described previously was used, except the NK-92 cells were pre-treated for 3 hours with 5 μM of the broad range MMP inhibitor, GM6001, in NK-92 cell media prior to incubation with the hydrogels. During

the incubation period, the media was maintained with 5 μM of GM6001. For the integrin binding to soluble RGD study, the same experimental set up as described previously was used, except the NK-92 cells were pre-treated for 2 hours with media containing 0.5 mM RGD peptide, prior to incubation with the hydrogels. During the incubation period, the media was maintained with 0.5 mM of RGD peptide. The control group for these studies was the group 2 hydrogel with incubation of untreated NK-92 cells. At the end of 7 days, the NK-92 cells were stained with calcein AM and the hydrogels were rinsed in PBS, imaged with confocal microscopy, and analyzed, as described previously.

Effects of SDF-1α on NK-92 Cell Gene Expression:

The effect of SDF-1α on MMP and integrin expression in NK-92 cells was evaluated by quantitative real-time PCR after incubation of NK-92 cells in NK-92 cell media (with IL-2) with 100 ng/mL SDF-1α for 24 hours. RNA was extracted from the cells using RNeasy Mini Kit (Qiagen, Hilden, Germany) per manufacturer's instructions and converted to cDNA (iScript™ cDNA synthesis kit; Bio-Rad, Hercules, CA, USA), per manufacturer's instructions on the Mastercycler® nexus (Eppendorf, Hamburg, Germany). Quantitative RT-PCR was then performed on an Applied Biosystems™ QuantStudio™ 6 Flex Real-Time PCR System (Applied Biosystems, Life Technologies, Carlsbad, CA, USA) using fast SYBR™ green master mix (Applied Biosystems, Life Technologies, Carlsbad, CA, USA). Relative expression levels of target genes were determined using the comparative C_T method. The primer sequences for all MMP and integrin subunit target genes are listed in Supplementary Table S1 (Eurofins Genomics, Luxembourg City, Luxembourg). Target gene expression was normalized to GAPDH. Control NK-92 cells in NK-92 cell media (with IL-2) were used for baseline gene expression. Three independent experiments were performed, each with a sample size of 3.

Tumor Model Formation:

A549 or H1299 cancer cells were photoencapsulated at 10 million cells/mL in 10 μL of the group 2 hydrogel (Table 1) composition (50:50 ratio of 10% (w/v) PEG-DA and 10% (w/v) PEG-dMMP-PEG, and 5 mM PEG-RGD), dissolved in PBS with 0.05% (v/v) photoinitiator. The tumor models were polymerized as described previously, rinsed in PBS, cancer cell media was added, and the tumor models were cultured over time. The tumor models had an average diameter of 2.7 ± 0.26 mm.

Cancer Cell Viability and Proliferation in the Tumor Models:

Cell viability was assessed by live/dead assay following manufacturer's instructions. Tumor models were rinsed with PBS and stained with calcein AM and ethidium bromide-1 for 1 hour at room temperature immediately after encapsulation (day 0), and on days 1 and 7. After staining, tumor models were rinsed in PBS and imaged with confocal microscopy. Cell proliferation within the tumor models was assessed by MTS assay on day 0, day 1, and every other day up to day 13. The tumor models were added to 100 μL of fresh cancer cell media and 80 μL of MTS reagent and incubated for 1 hour. The media was collected and measured for absorbance at a wavelength of 490 nm (Biotek, Synergy HT Microplate Reader, Winooski, VT, USA). Brightfield images of the tumor models were taken with an EVOS XL Core microscope (Invitrogen, Carlsbad, CA, USA). To further characterize the cancer cell number and growth, tumor models at 1 day and 7 days after cell encapsulation were rinsed in PBS and stored at -80°C until use for DNA quantification. Each tumor model was homogenized (Bio-Gen Series PR-200 Homogenizer; Pro Scientific, Oxford, CT, USA) for 2 minutes in 1X Reporter Lysis Buffer. The DNA content was quantified using Quant-iT^{TM} PicoGreen^{TM} dsDNA assay kit following

manufacturer's instructions. Tumor models on day 1 are considered to be at an "early stage" of growth and on day 7 are considered "late stage".

Mechanical Characterization of Tumor Models:

The A549 or H1299 cancer cells were photopolymerized at 10 million cells/mL, in the group 2 PEG precursor solution (Table 1) previously used for tumor models, in cylindrical silicon molds (Grace Biolabs) 8 mm diameter by 1.7 mm depth, as described previously. The viscoelastic properties of early and late stage tumor models were examined using an Anton Paar MCR 302 rheometer with parallel plate geometry according to established methods[56,57] and as described previously. Then the Young's moduli of the tumor models were determined as described previously. For each cell type and time point, 3 tumor models were used for the amplitude sweeps and 4 tumor models were used for the frequency sweeps.

Stress-Induced Ligand Expression on Cancer Cells in Tumor Models:

Early and late stage tumor models were fixed with 4% paraformaldehyde overnight, rinsed, and stored in PBS at 4°C until use. The samples were permeabilized with 0.1% (v/v) Triton X-100 in PBS at 37°C on a shaker overnight, followed by blocking with 10% goat or donkey serum for 8 hours. Samples were then incubated with the primary antibody for the stress-induced ligands MICA/B or ULBP1 (1:100 dilution in 1% serum, for both) at 37°C on a shaker for 24 hours, followed by washing and overnight incubation in PBS on a shaker at 37°C. The tumor models were then incubated with a FITC tagged donkey anti-rabbit or goat anti-mouse secondary antibody (1:100 dilution in 1% serum, for both) at 37°C on a shaker for 24 hours, followed by washing and incubation with PBS overnight. The samples were counterstained with Hoescht 33258 dye for 3 hours at 37°C on a shaker, rinsed in PBS, and imaged with confocal microscopy.

Evaluation of Cancer Cell Cytokine and Chemokine Production in 2D and 3D Cultures:

On day 0, A549 and H1299 cells were seeded in 2D monolayer at the same cell number in the tumor models, or encapsulated in the tumor models at 10 million cells/mL. On day 1, NK-92 cell media was added to the 2D cancer cells and 3D early stage tumor models for 6 hours. The media was collected, centrifuged at 1000 rpm for 5 minutes to remove any cells, and stored at -80°C until testing. The samples were tested to determine the concentration of MICA and cancer cell related cytokines and chemokines listed in Supplementary Table S2 using ELISAs, per manufacturers' instructions. Results from the ELISAs were also normalized to the cancer cells' total DNA in the sample.

In a separate study, the media from the migration study (described in the next section) was collected, centrifuged to remove any cells, and stored at -80°C until testing for cancer cell related cytokines and chemokines and MICA, listed in Supplementary Table S2, by ELISAs, per manufacturers' instructions. The controls included NK-92 cell media collected after 2 hours from the tumor models alone and NK-92 cells alone. Results from the ELISAs were also normalized to the cancer cells' total DNA in the sample.

Evaluation of NK-92 Cell Migration into Tumor Models:

Cancer cells were stained with 1 μL/mL of DiI in cancer cell media for 2 hours prior to encapsulation in the hydrogel at 10 million cells/mL. The stained early or late stage tumor models were incubated with 50,000 calcein AM labeled NK-92 cells (a defined effector to target (E:T) cell ratio of 0.5:1 for early stage models) for 2 hours in NK-92 cell media with IL-2, on a shaker at 50 rpm (Scheme 1). NK-92 cell labeling was achieved by adding 0.5 μL/mL calcein AM in NK-92 cell media to the cells for 2 hours then rinsed in PBS prior to incubation with the models. After incubation, the media was collected for ELISAs and the tumor models were rinsed

with PBS and imaged with confocal microscopy. The images were analyzed for migration distance and mean fluorescence values using Fiji.[64]

To investigate if cell density in the tumor model impacts NK-92 cell migration, DiI stained A549 or H1299 cancer cells were encapsulated in the hydrogels at 10 million cells/mL and 20 million cells/mL. The stained early stage tumor models at the different cell densities were incubated with calcein AM labeled NK-92 cells at an E:T cell ratio of 0.5:1 in NK-92 cell media, on a shaker at 50 rpm. After 2 hours of incubation, the tumor models were rinsed in PBS, imaged with confocal microscopy, and analyzed for NK-92 cell migration by mean fluorescence values using Fiji.[64]

To further probe the role of TGF- β signaling in the tumor models on NK-92 cell migration, NK-92 cells were pre-treated with a small molecule inhibitor of TGF-β receptor I (TGFBRI) (LY2157299) for 24 hours and labeled with calcein AM during the last 2 hours of treatment with the inhibitor. The NK-92 cells were then rinsed in PBS and incubated with the DiI stained (as previously described) early and late stage tumor models at an E:T ratio of 0.5:1

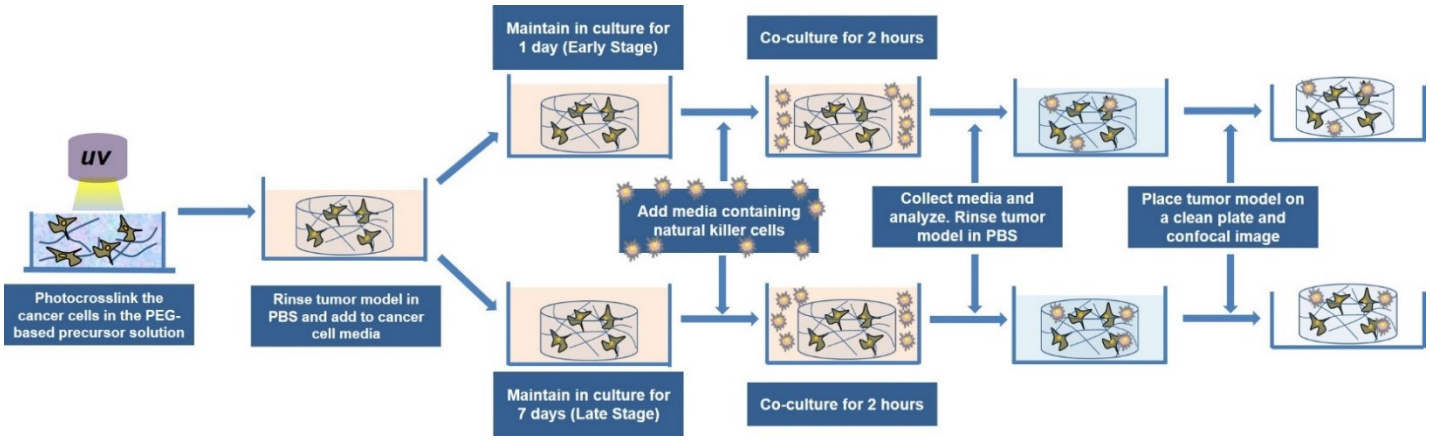

Scheme 1. Method for NK-92 cell incubation with early and late stage tumor models. Cancer cells were encapsulated into the hydrogels and cultured for 1 or 7 days. On that day, the tumor models were incubated with media containing 50,000 NK-92 cells. After two hours, the media was collected for cytokine and chemokine analysis, then the tumor models were rinsed in PBS, and placed on a clean plate for imaging.

(definable ratio only for early stage models), in NK-92 cell media (with IL-2), on a shaker. Controls for this study include the DiI stained (as previously described) early and late stage tumor models incubated with untreated NK-92 cells, in NK-92 cell media (with IL-2), on a shaker. After 2 hours incubation, the tumor models were rinsed in PBS, imaged with confocal microscopy, and analyzed for NK-92 cell migration by mean fluorescence values using Fiji.[64]

NK-92 Cell-Mediated Cytotoxicity in 2D and 3D Cultures

For the 2D monolayer NK-92 cell-mediated cytotoxicity, 30,000 A549 and H1299 cancer cells were plated in a 96 well plate on day 0. On the same day, 3D tumor models were made with cancer cells at a density of 10 million cells/mL, as described previously. On day 1, the 2D culture and 3D tumor models were incubated with NK-92 cells at an E:T cell ratio of 0.5:1 or 1:1 for 2 hours in 200 µL of Opti-MEM media with 1% (v/v) ITS Premix Universal Culture Supplement, 1% (v/v) penicillin-streptomycin, and 100 units/mL IL-2, on a shaker at 50 rpm. On day 7, the process was repeated for the 3D tumor models, with the same number of NK-92 cells used with the day 1 tumor models (for both E:T cell ratios; 0.5:1 50,000 NK-92 cells and 1:1 100,000 NK-92 cells). After 2 hours of incubation, the media was removed, centrifuged at 1000 rpm for 5 minutes to remove any cells, the supernatant was removed and mixed, and then 100 µL was plated in black 96 well plate and allowed to cool to room temperature. Then the CytoTOX-ONE™ Homogeneous Membrane Integrity Assay (lactate dehydrogenase assay, LDH assay) was performed, per manufacturers' instructions. The controls were NK-92 cells alone (same number of cells), cancer cells or tumor models alone, cancer cell or tumor model lysate, and media alone. NK-92 cell-mediated cytotoxicity was determined by Equation (4).

$$Cytotoxicity\ (\%) = 100 \times \frac{(Experimental - NK{-}92\ cells{+}media\ background)}{(Maximum\ LDH\ Release - Culture\ media\ background)} \quad (4)$$

Evaluation of NK-92 Cell Cytokines and Chemokines in Response to Cancer Cell in 2D and 3D Cultures:

On day 0, A549 and H1299 cells were seeded in 2D monolayer, at the same cell number in the tumor models, or encapsulated in the tumor models at 10 million cells/mL. On day 1, NK-92 cells were added at an E:T ratio of 0.5:1 in NK-92 cell media supplemented IL-2, on a shaker at 50 rpm. After 2 hours, the media was collected, centrifuged at 1000 rpm for 5 minutes to remove the cells, and stored at -80°C until testing. ELISAs were performed to determine the amount of IFN-γ produced by the NK-92 cells in response to the cancer cells and tumor models. The controls were media collected after 2 hours from the cancer cells alone, tumor models alone, and NK-92 cells alone.

The media from the migration studies, as described previously, was collected, centrifuged to remove any cells, and stored at -80°C until testing for NK-92 cell related cytokines and chemokines, listed in Supplementary Table S2, by ELISAs, per manufacturers' instructions. The controls included NK-92 cell media collected after 2 hours from the tumor models alone and NK-92 cells alone.

Evaluation of NK-92 Cell Gene Expression after Exposure to Tumor Model Conditioned Media:

Conditioned media studies were performed to study how factors secreted from the tumor models affected MMP and integrin expression in NK-92 cells. The early and late stage tumor models were placed in fresh NK-92 cell media. After 2 hours, the media was collected and centrifuged to remove any cells, now referred to as conditioned media (CM). The CM with IL-2 was added to NK-92 cells and incubated for 2 hours. RNA was extracted from the cells, cDNA synthesized, and quantitative RT-PCR was performed, as described previously. The primer sequences for all target genes are listed in Supplementary Table S1. Target gene expression was

normalized to GAPDH. Control NK-92 cells in fresh NK-92 cell media for 2 hours was used for baseline gene expression. Three independent experiments were performed, each with a sample size 3.

Confocal Microscopy:

For all confocal imaging, a Zeiss LSM 710 confocal microscope in scanning mode was used (Carl Zeiss, Oberkochen, Germany). The microscope had a diode (405 nm), Argon (458 nm, 488 nm, 518 nm), and HeNe (543 nm, 594 nm, 633 nm) laser modules. Images were acquired using the ZEN imaging software (Carl Zeiss, Oberkochen, Germany).

Statistics:

GraphPad Prism (GraphPad Software, San Diego, CA, USA) was used to perform statistical analyses. For experiments with 1 independent variable and 2 groups, a Student's t-test was performed. For experiments with 1 independent variable and more than 2 groups, a one-way ANOVA and post hoc analysis with Tukey correction was performed to identify differences between groups. For experiments with 2 independent variables (i.e. cell type and stage), a two-way ANOVA was performed followed by post hoc analysis with Tukey's correction when the interaction P value was ≤ 0.05, otherwise, the P values for the main effects were used to determine statistically significant differences between groups. For experiments in which outcomes were compared to baseline values, the respective ANOVA followed by post hoc analysis with a Dunnett's correction was performed. For experiments with 3 independent variables (i.e. cell type, stage, and NK-92 cell treatment), a three-way ANOVA and post hoc analysis with Tukey correction was performed to identify differences between groups. Statistical significance was considered as $P \leq 0.05$. All numerical data are shown as individual experimental sample points, with the mean ± standard deviation of the mean overlaid on the graph.

Results

Characteristics of PEG-Based Hydrogels for Evaluating NK-92 Cell Migration

To probe the requirements for NK-92 cell migration, PEG-DA hydrogels were engineered with and without MMP degradable sites and different concentrations of RGD, or a control RAD peptide, while maintaining similar mechanical and physical properties. The six different hydrogel compositions had comparable Young's moduli, of 27 to 43 kPa (Figure 1A), which coincides with reported values for lung tumors *in vivo*, of 20-150 kPa.[65–69] The swelling ratios of the hydrogels were also comparable (Figure 1B), which suggests similar crosslinking densities[70,71] and mesh sizes[72] among the different hydrogel compositions. Furthermore, the biochemical, physical, and mechanical properties of these PEG-based hydrogels are consistent with previous hydrogels for lung and other solid tumor models.[25,26,73]

To promote NK-92 cell migration into the hydrogels, a chemoattractant point source was required (Figure S1). As such, a point source of 100 ng of SDF-1α was encapsulated into the hydrogels. Quantification of release indicated 1 ng of the SDF-1α was detected in the media over 7 days (Figure 1C), which was effective in stimulating NK-92 cell migration (Figure S1 and

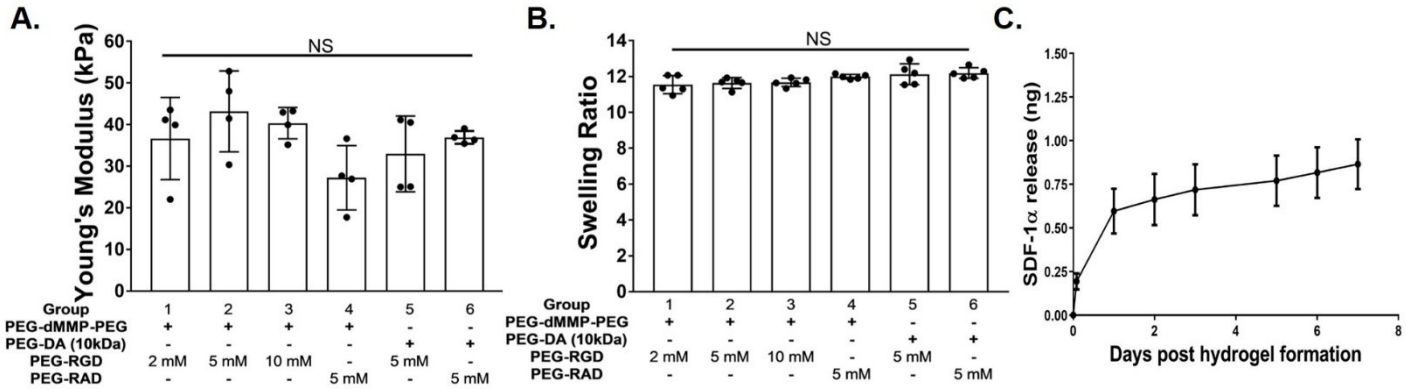

Figure 1. Characterization of PEG-based hydrogels. (**A**) Young's modulus (n=4) and (**B**) swelling ratio (n=5) of PEG-based hydrogels with or without an MMP degradable peptide and varying concentrations of RGD, or RAD negative control peptide. NS denotes no significance. (**C**) The amount of SDF-1α released from a 100 ng fibrin clot point source in the hydrogel (group 2 composition) into the media over 7 days (n=3).

Figure 2A).

NK-92 Cell Migration into PEG-Based Hydrogels

These six hydrogel compositions enabled us to study the effects of MMPs and integrins on NK cell migration, while keeping mechanical and physical properties of the gel constant. NK-92 cell migration was observed from all directions into the hydrogel, but migration distance was measured from the side edges. For reference, the hydrogels were 5100 μm in diameter and the distance from the edge of the gel to the point source was approximately 2500 μm. The six hydrogel compositions supported NK-92 cell infiltration (Figure S2), however, the amount of infiltrating cells and the distance of migration were dependent on the presence of MMP degradable sites and the concentration of RGD adhesion sites (Figure 2A, 2B, and 2C). The highest amounts of infiltrating NK-92 cells, based on the fluorescent intensity of NK-92 cells in the gel, were observed in the MMP degradable hydrogels with 5 mM and 10 mM RGD (group 2 and 3, Figure 2B). However, the NK-92 cells migrated 200 μm farther into the 10 mM RGD hydrogels than in the 5 mM RGD hydrogels, which corresponded to maximum migration distances of 1475 μm and 1275 μm, respectively (Figure 2C). In comparison, the amount of infiltrating NK-92 cells in the MMP degradable hydrogels containing 2 mM RGD (group 1) was 3.8- and 4.1-fold lower than the amounts into the corresponding gels with 5 mM and 10 mM RGD, respectively. There was limited NK-92 cell migration into the MMP degradable gels with 2 mM RGD, with most cells observed within 75 μm from the edge of the hydrogels and the maximum migration distance (675 μm) was approximately half that of MMP degradable gels with 5 or 10 mM RGD. These findings demonstrate that the maximum migration distance of NK-92 cells correlated with the concentration of RGD within the MMP degradable hydrogels, while the overall amount of infiltrating NK-92 cells plateaued at 5 mM RGD in the gels.

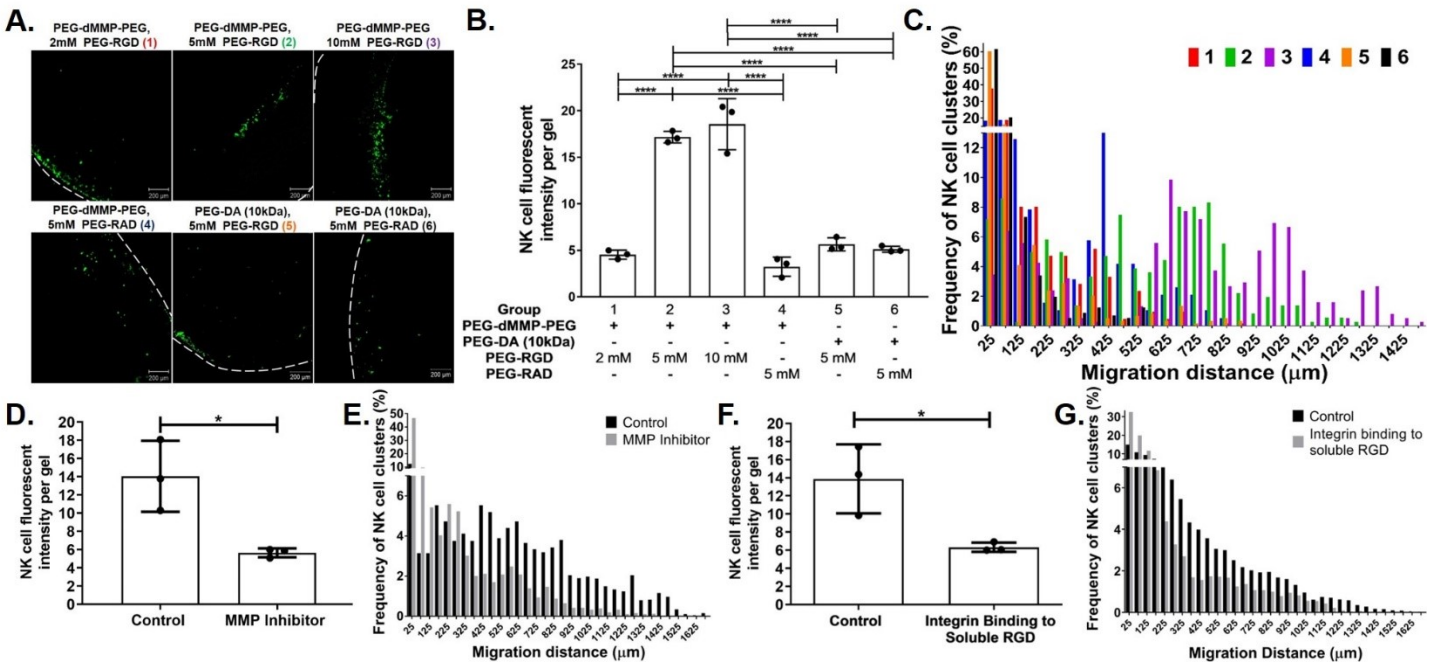

Figure 2. Migration of NK-92 cells into PEG-based hydrogels of different biochemical compositions. (**A**) Representative confocal microscopy images of calcein AM stained (green) NK-92 cells which migrated into various compositions of the PEG based hydrogels (Groups are the same as in Figure 1) (n=3, average diameter 5.1 ± 0.09 mm). (**B**) Total fluorescent intensity of NK-92 cells in the hydrogels and (**C**) frequency of NK-92 cell clusters at increasing migration distances (groups are the same as in A) (n=3). (**D**) Total fluorescent intensity of NK-92 cells and (**E**) frequency of NK-92 cell clusters at increasing migration distances in the PEG-dMMP-PEG, 5 mM PEG-RGD gels (group 2) with and without the presence of an MMP inhibitor (GM6001) (n=3). (**F**) Total fluorescent intensity of NK-92 cells and (**G**) frequency of NK-92 cell clusters at increasing migration distances in the PEG-dMMP-PEG, 5 mM PEG-RGD gels (group 2) with and without the presence of soluble RGD in the media (n=3). For (B), (D) and (F), * denotes $P \leq 0.05$ and **** denotes $P \leq 0.0001$

Substitution of the MMP degradable PEG-DA with a non-degradable PEG-DA decreased NK-92 cell migration, in terms of the amount of infiltrating cells and maximum migration distance. In the non-degradable hydrogels with 5 mM RGD (group 5), the amount of infiltrating NK-92 cells decreased by 3-fold relative to the MMP degradable 5 mM RGD hydrogels (group 2, Figure 2B). Similarly, the maximum migration distance by the NK-92 cells decreased by 400 μm in the non-degradable hydrogels with 5 mM RGD, relative to the degradable gels with 5 mM RGD, distances of 875 μm and 1275 μm (Figure 2C). The amount of

infiltrating NK-92 cells in the non-degradable gels with 5 mM RAD (group 6) was comparable to the amount in the MMP degradable gels with 5 mM RAD (group 4). In non-degradable gels with 5 mM RAD, the majority of NK-92 cells were observed within 75 μm from the edge of the gel, suggesting limited migration, and the maximum migration distance (525 μm) was 200 μm less than into the degradable gels with 5 mM RAD. Going forward, studies were conducted using the MMP degradable hydrogels containing 5 mM RGD, which was supportive of NK-92 cell migration and consistent with other studies utilizing PEG-based hydrogels for various tumor models.[25,26]

To further elucidate if NK cell migration was MMP-dependent, the experiment was repeated in MMP degradable hydrogels containing 5 mM RGD in the presence of the broad range MMP inhibitor, GM6001. Inhibition of MMPs in NK-92 cells decreased the amount of infiltrating cells by 2.5-fold relative to the amount of infiltrating control NK-92 cells (Figure 2D). Additionally, inhibition of MMPs in NK-92 cells decreased their maximum migration distance relative to that of control NK-92 cells, and the majority of the inhibited cells were observed within 75 μm from the edge of the hydrogel (Figure 2E). This study corroborated the findings from the NK-92 cell migration into non-degradable hydrogels, demonstrating the importance of MMPs in NK-92 cell migration.

To further elucidate the integrin-dependence of NK cell migration, experiments were repeated in MMP degradable hydrogels containing 5mM RGD, but this time with NK-92 cells pre-incubated with soluble RGD. Occupying integrin receptors with soluble RGD significantly decreased the amount of infiltrating NK-92 cells by 2.2-fold (Figure 2F) and decreased the maximum migration distance relative to control cells (Figure 2G). Indeed, in the presence of soluble RGD the majority of NK-92 cells were observed within 75 μm from the edge of the

hydrogel. This study further suggests that integrin binding to the hydrogel is important for NK-92 cell migration.

Since NK-92 cell migration into the hydrogels was dependent on the inclusion of SDF-1α, the presence of MMP degradable sites and concentration of integrin adhesion sites, we hypothesized the chemokine influenced MMP and integrin expression in the NK-92 cells. However, treating NK-92 cells with SDF-1α and IL-2 did not, on average, change the gene expression profiles of soluble or surface bound MMPs compared to NK-92 cells stimulated with IL-2 alone (Figure S3). Furthermore, the SDF-1α treated NK-92 cells did not show a change in gene expression of integrin subunits, which adhere to the RGD sites in the hydrogel, except for an increase in the β5 subunit gene.

Cancer Cell Characteristics in the Tumor Models

The non-metastatic A549 and metastatic H1299 cancer cell lines were successfully photoencapsulated into hydrogels and remained viable (Figure S4). The A549 and H1299 cancer cells displayed similar trends in metabolic activity over the 13 days cultured in the hydrogels (Figure 3A). Both cell lines proliferated in the hydrogels and exhibited a significant increase in metabolic activity by day 7 in culture until day 13, relative to day 0. Tumor models at two stages of growth were selected to study the evolution of the microenvironment over time – day 1 for early stage and day 7 for late stage. Late stage was chosen as day 7 because the cells in the hydrogel were still viable (Figure 3B), but had plateaued in terms of metabolic activity at subsequent time points (Figure 3A). Indeed, there was no significant difference in metabolic activity between day 7 and each of the following days for A549 or H1299 models (all $p>0.99$). The DNA content in the tumor models at early stage and late stage corroborated the results from the MTS assay (Figure 3C). The early stage models had comparable DNA content, while the late

stage models had significantly more DNA than the respective early stage models. Additionally, the late stage H1299 model had significantly more DNA content than the late stage A549 model. Brightfield microscopy showed the formation of cell clusters in the late stage A549 and H1299 tumor models, compared to their respective early stage (Figure 3D).

To determine if mechanical characteristics of the tumor models evolved with time, the Young's modulus of each tumor model was determined at early stage and late stage (Figure 3E). At early stage, the A549 and H1299 tumor models had comparable Young's moduli, in the softer end of the range of reported values for lung tumors *in vivo.*[65–69] The Young's modulus of the late stage A549 tumor model increased by 45% relative to the A549 early stage, while the H1299 tumor models at both stages had comparable moduli. Additionally, the Young's modulus of the late stage A549 tumor model was significantly higher than that of the late stage H1299 tumor model.

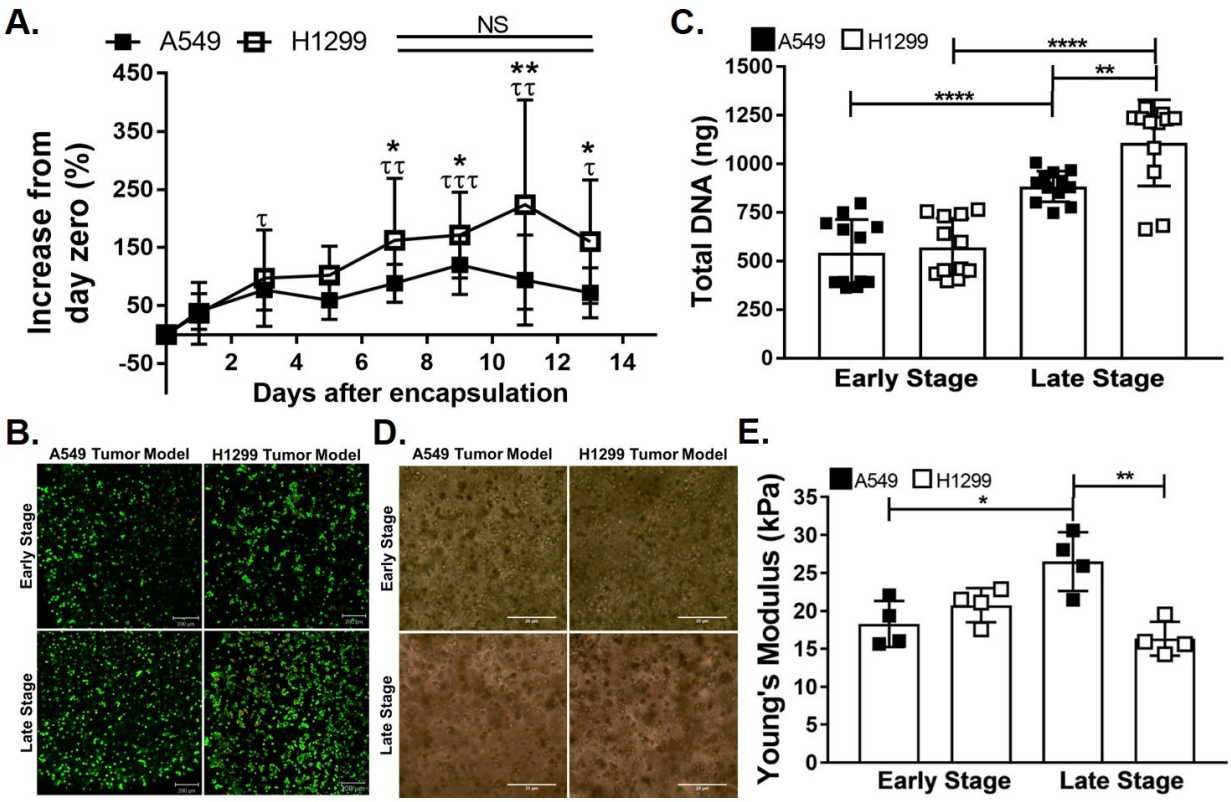

Figure 3. Characteristics of A549 and H1299 cells in the tumor models over time. (**A**) Proliferation of cancer cells over time in the tumor models, determined by MTS assay, as a percent increase from the day of encapsulation (day 0) until 13 days after encapsulation (n=6). Significant differences from day 0 within each tumor model are noted; for A549 tumor models, τ denotes $P \leq 0.05$, ττ denotes $P \leq 0.01$, and τττ denotes $P \leq 0.001$; for H1299 tumor models, * denotes $P \leq 0.05$ and ** denotes $P \leq 0.01$. For comparisons between day 7 and each of the following days (days 9, 11, and 13), NS denotes no significance in either tumor model. (**B**) Live/dead stain for the viable (green) and dead (red) cells encapsulated within the tumor models at the early (day 1) and late (day 7) stage (n=3). (**C**) Total DNA from each tumor model at early and late stages (n=12). (**D**) Brightfield images for the tumor models at early and late stage, demonstrating spheroid formation at the late stage (n=3). (**E**) Young's modulus of the tumor models at early stage and late stage determined by rheology (n=4). For (C) and (E), * denotes $P \leq 0.05$, ** denotes $P \leq 0.01$, and **** denotes $P \leq 0.0001$.

Immunomodulatory Molecules Produced by the Tumor Models

To determine if the 3D hydrogel culture system affects the production of soluble immunomodulatory molecules by the cancer cells, we evaluated stress ligand shedding and cytokine and chemokine production by non-metastatic A549 and metastatic H1299 cells in a 2D monolayer and in the 3D PEG-based hydrogels after one day in culture, normalized to DNA content (Figure S5). The two lung cancer cell lines had different profiles of soluble

immunomodulatory molecules production in 2D cultures; compared to the A549 cells, the H1299 cells shed 14.3-fold higher levels of the stress ligand MICA (Figure S5A), produced 3.1-fold more of the immunosuppressive cytokine TGF- β (Figure S5B), 2.2-fold less of the pleiotropic cytokine IL-6 (Figure S5C), and 2.2-fold less of the chemokine MCP-1 (Figure S5D). The differences between the soluble molecules produced by the two cancer cells in 2D cultures were comparable to the differences observed between the cancer cells cultured in the early stage 3D tumor models. Indeed, compared to the A549 tumor model, the H1299 tumor model exhibited 5.5-fold greater MICA shedding, 3.7-fold greater production of TGF-β, and 2.6-fold less production of IL-6 and MCP-1. Overall, however, the levels of MICA, TGF-β, IL-6, and MCP-1 tested were lower in the 3D tumor models relative to 2D culture. The production of two other chemokines, SDF-1α and CX3CL1, was comparable between the different cultures and cell types (Figure S5E and S5F). The difference between the 2D and 3D cultures may be due to proteins binding to or being trapped in the gel,[74,75] or the production of these factors may be lower on a per cell basis in the tumor model. Nevertheless, these data suggest that the two cell lines of different metastatic potential have different profiles of soluble immunomodulatory molecules prior to encapsulation in the tumor models, and these differences are maintained in the 3D tumor models.

The expression of immunomodulatory molecules was further evaluated in subcutaneous xenografts of A549 and H1299 cell lines. Here we observed increased expression of TGF-β2, TGF-β3, IL-6, MCP-1, and CX3CL1, and decreased TGF-β1 expression in the H1299 xenografts relative to the A549 xenografts (Figure S6). The expression of SDF-1 was similar between the H1299 and A549 xenografts. Differences in growth kinetics and the influence of other cell types *in vivo* make it challenging to draw comparisons between *in vivo* and *in vitro* culture conditions. Despite these limitations, there were consistent differences between the two cell lines in 2D cultures, the 3D tumor models, and xenografts, primarily in the overall TGF-β production, and the IL-6 and SDF-1 production. The increased proliferation of the H1299 cells relative to the A549 cells was consistent across xenografts (Figure S6H) and 3D tumor models (Figure 3A and 3C). Overall, these findings demonstrate that the cell lines have different immunomodulatory characteristics *in vitro* and *in vivo* that are consistent in many respects with the 3D tumor models.

The tumor models were then evaluated for the presentation of stress-induced ligands, MICA/B and ULBP1, which are primarily associated with NK cell recognition of transformed cells via the key activating receptor, NKG2D.[2] Both the non-metastatic A549 and metastatic

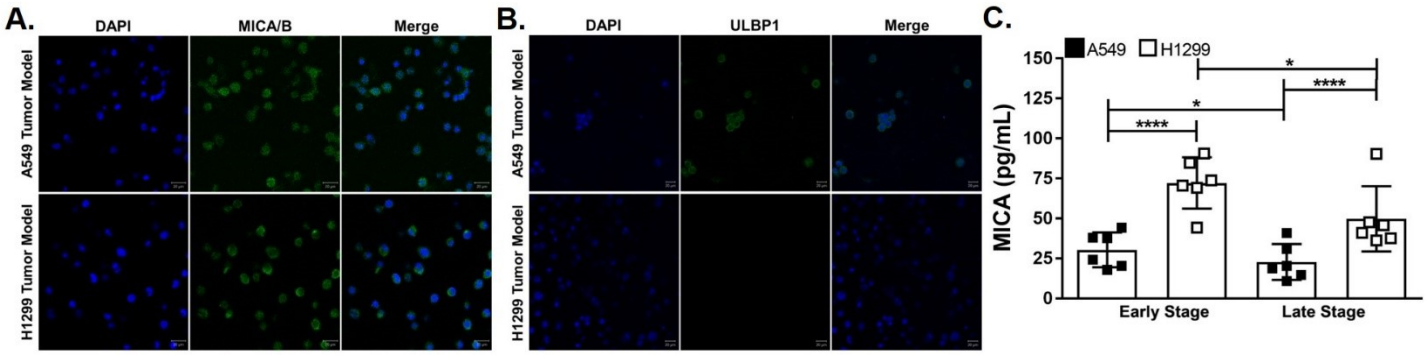

Figure 4. Expression and shedding of stress-induced ligands in the tumor models for the NK cell activating receptor NKG2D. Representative images for immunofluorescent staining of (**A**) MICA/B (green) and (**B**) ULBP1 (green) in the early stage A549 and H1299 tumor models, with cell nuclei stained with Hoechst (blue) (n=3). (**C**) The concentration of MICA shed into the media in the A549 and H1299 tumor models at both stages (n=6); * denotes $P \leq 0.05$ and **** denotes $P \leq 0.0001$.

H1299 cells expressed MICA/B in early and late stage tumor models (Figure 4A and S7A). However, while A549 cells expressed ULBP1 at both stages, the expression of this stress ligand was downregulated by H1299 cells in both early and late stage models (Figure 4B and S7B). While the shedding of MICA was observed in both tumor models, this occurred to a greater extent (~2-fold) in the H1299 models compared to A549 models, at both stages (Figure 4C). Surprisingly, there was a slight decrease in the amount of MICA shed by the late stage models, relative to the corresponding early stage tumor models.

Analysis of soluble immunomodulatory molecules in the tumor models revealed differences across lung cancer cell type and growth. TGF-β, a well-known immunosuppressive factor, was produced at higher levels by the metastatic H1299 tumor models compared to the non-metastatic A549 models at both early and late stages, by 8.2- and 4.1-fold respectively (Figure 5A). There was an overall increase in TGF-β with time in culture, with

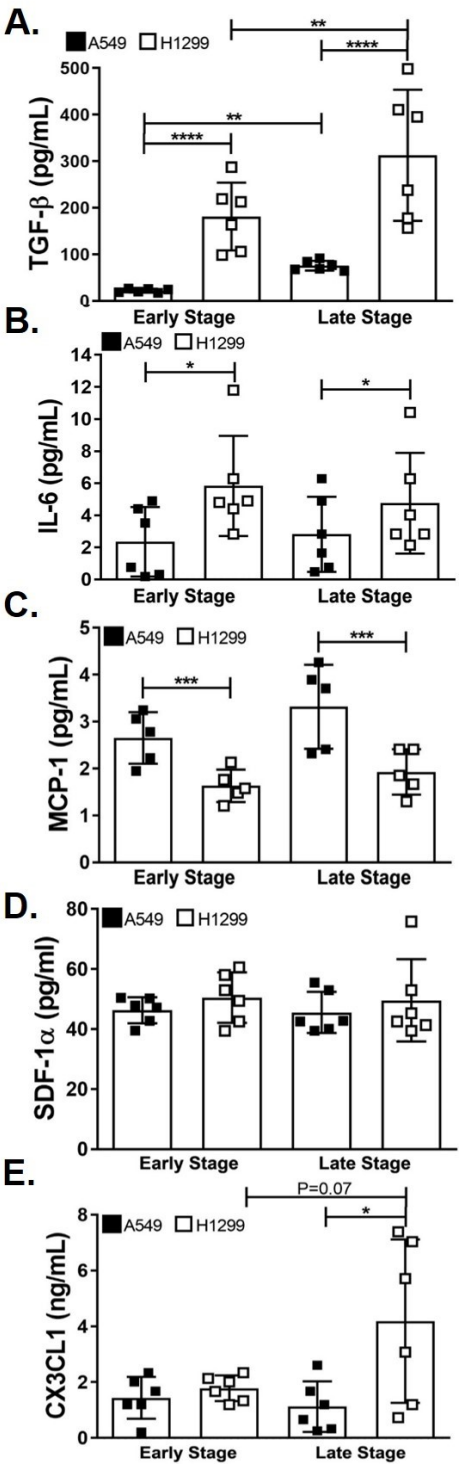

Figure 5. Cytokine and chemokine production by the tumor models. ELISAs were used to determine the concentration of (**A**) TGF-β, (**B**) IL-6, (**C**) monocyte chemoattractant protein 1 (MCP-1), (**D**) stromal cell-derived factor 1α (SDF-1α), and (**E**) chemokine (C-X3-C motif) ligand 1 (CXC3L1) in the media of the A549 and H1299 tumor models at the early and late stage (n=6, except for MCP-1 n=5). * denotes $P \leq 0.05$, ** denotes $P \leq 0.01$, *** denotes $P \leq 0.001$, and **** denotes $P \leq 0.0001$.

the late stage A549 tumor model producing 3.4-fold more TGF-β than the early stage A549 model, and the late stage H1299 model producing 72.6% more TGF-β than the early stage H1299 model. The production of the pleiotropic cytokine IL-6 was dependent on the cell type within the tumor model (Figure 5B). The H1299 tumor model produced 2.5-fold and 68.8% more IL-6 than the A549 model at early and late stage, respectively. The production of chemoattractant proteins by the tumor models was also evaluated, including MCP-1, SDF-1α, and CX3CL1. The production of MCP-1 was again dependent on the cell type within the tumor models, with the A549 tumor models producing more of this chemokine by 62.5% and 72.1% than the H1299 models at early and late stage, respectively (Figure 5C). In the case of SDF-1α, production was comparable across the models and stages (Figure 5D). For CX3CL1, the early stage and late stage A549 models produced comparable amounts, but the late stage H1299 model produced 3.7-fold more relative to the late stage A549 tumor model (Figure 5E).

Since there was a significant increase in metabolic activity and DNA content in the tumor models over the 7 day culture period, the production of soluble immunomodulatory molecules was also normalized to DNA content (Figure S8). These data showed similar trends to the un-normalized data. This suggests that the increase in TGF-β production with time in culture was not a consequence of an increase in cell number, but rather an increase in the production of the cytokine per cell. These findings also demonstrated that differences in MICA shedding, TGF-β, MCP-1, and CX3CL1 production observed between the two cell lines in the tumor models are a result of differences in cell phenotype, and not cell number. In the case of IL-6, a similar trend was observed though statistical significance was lost ($p=0.07$) upon normalization to DNA; therefore, IL-6 production may not be a distinguishing characteristic between A549 and H1299 cells. This was not surprising given its pleiotropic role in the tumor microenvironment.[23,76]

NK-92 Cell Migration into the Tumor Models

Migration of NK-92 cells into the tumor models was studied to determine how differences in soluble immunomodulatory molecules influence NK-92 infiltration. The extent of NK-92 cell migration into tumor models, in terms of amount (based on fluorescence intensity of NK-92 cells), migration distance, and colocalization with the cancer cells, was dependent on the cell type and stage (Figure 6). For comparison, representative fluorescent images of tumor models without NK-92 cell incubation are shown in Figure S9. NK-92 cells migrated to a greater extent, in terms of amount and distance, into the early stage tumor models compared to the late stage, for both A549 and H1299 models. The amount of infiltrating NK-92 cells was 3.2-fold greater and the average migration distance was 75% farther in the early stage

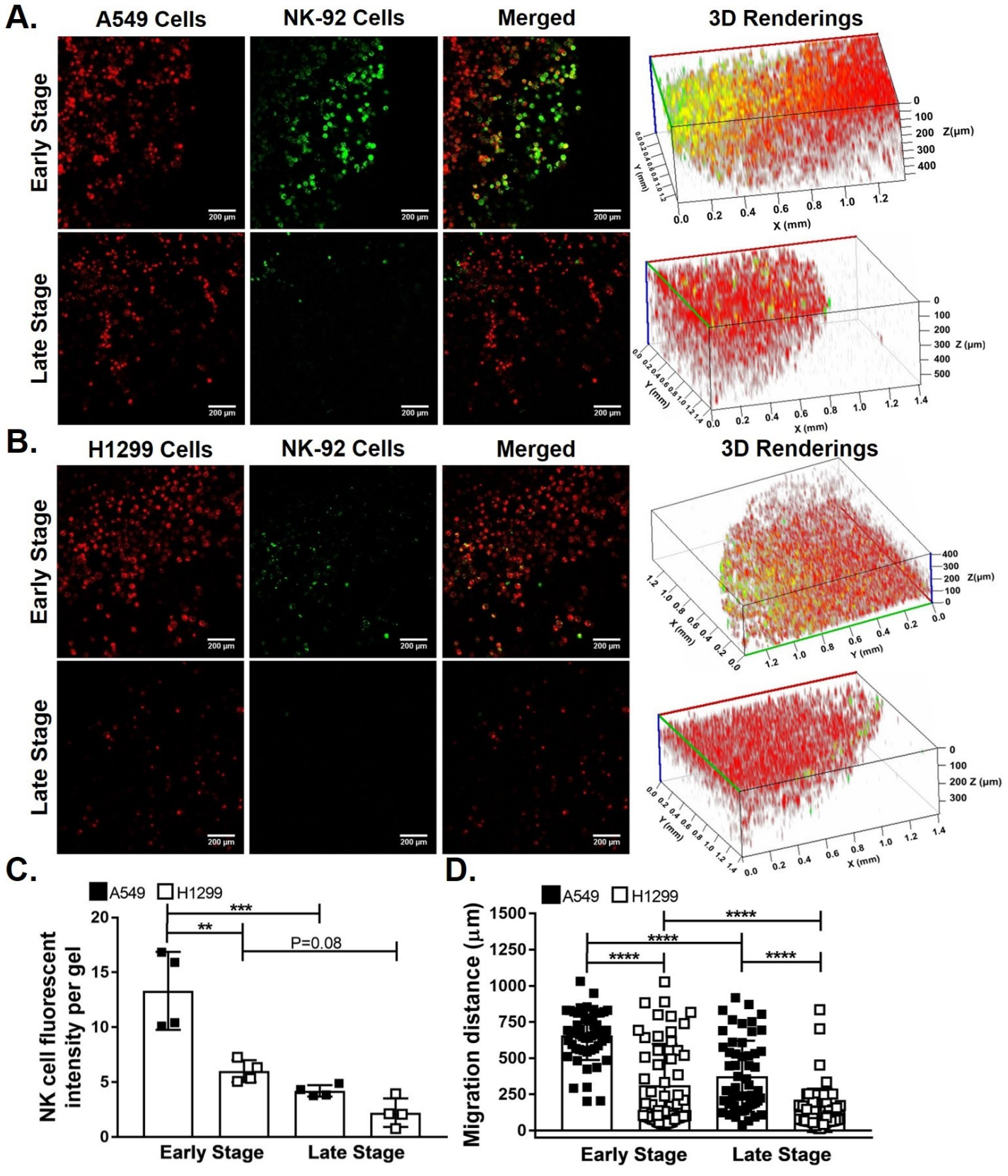
A.
A549 Cells
NK-92 Cells
Merged
3D Renderings
Early Stage
Late Stage
200 µm
Z(µm)
X (mm)
Y (mm)
B.
H1299 Cells
NK-92 Cells
Merged
3D Renderings
Early Stage
Late Stage
200 µm
Z (µm)
X (mm)
Y (mm)
C.
A549
H1299
NK cell fluorescent intensity per gel
***
**
P=0.08
Early Stage
Late Stage
D.
A549
H1299
Migration distance (µm)
****
****
****
****
Early Stage
Late Stage

Figure 6. Migration of NK-92 cells into the A549 and H1299 tumor models. Migration of NK-92 cells (green) into early and late stage (**A**) A549 tumor models (red) and (**B**) H1299 tumor models (red). 2D images and corresponding 3D renderings spanning the entire height of the tumor models. The diameter of the tumor models was 2.7 ± 0.26 mm; images were taken at a representative edge of the tumor model spanning approximately one quarter of the entire tumor model. (**C**) Fluorescent intensity and (**D**) migration distance of the infiltrated NK-92 cells into the tumor models (n=4 gels). 60 representative measurements taken from the 4 gels for migration distance. ** denotes $P \leq 0.01$, *** denotes $P \leq 0.001$, and **** denotes $P \leq 0.0001$.

A549 tumor model than in the late stage A549 model (Figure 6C and 6D). This trend was observed, though less pronounced, in the H1299 models, where the amount of infiltrating NK-92 cells was 2.7-fold higher in the early stage model compared to the late stage model (p=0.08). The average migration distance of the NK-92 cells in the early stage H1299 tumor model was 2.2-fold farther relative to the late stage H1299 model. In the early stage models, the amount of infiltrating NK-92 cells and their average migration distance were ~2-fold greater in the A549 tumor model compared to the H1299 tumor model. In comparing late stage models, the amount of infiltrating NK-92 cells was similar between the A549 and H1299 models; however, the average migration distance was 2.7-fold greater in the A549 model compared to the H1299 model. In the 3D renderings of the tumor models with NK-92 cell migration, colocalization (yellow) was observed between the infiltrating NK-92 cells and the cancer cells. Qualitatively, there was greater colocalization between the NK-92 cells and the cancer cells in the early stage A549 tumor model compared to the early stage H1299 model. Furthermore, there was a marked decrease in colocalization of infiltrating NK-92 cells and the cancer cells in the late stage tumor models, relative to the early stage models, for both cell types.

To determine if cancer cell density alone was impacting NK-92 cell infiltration, a follow up study was performed, wherein A549 and H1299 tumor models at cell densities of 10 million cells/mL and 20 million cells/mL after 1 day of culture were incubated with NK-92 cells (Figure S10). These cell densities represent the cell density at the time of encapsulation and the

approximate cell density, based on the DNA assay (Figure 3C), after 7 days. These data showed no significant difference in NK-92 cell migration into the tumor models at different cell densities, suggesting that the decreased NK-92 cell migration in late stage models was not a consequence of the increased number of cancer cells within the tumor models

Functional Activity of NK-92 Cells during Co-Incubation with Cancer Cells in 2D and 3D

Natural killer cell function is commonly assessed by two effector mechanisms - cytotoxicity and production of cytokines and chemokines in response to a 2D culture of target cells. To understand how NK cell function differs in 3D co-culture systems relative to 2D systems, we compared NK-92 cell mediated cytotoxicity and production of IFN-γ during incubation with the cancer cells in a 2D culture and the 3D early stage tumor models, to maintain similar culture duration and cell number. Given that NK cell mediated cytotoxicity is determined by the totality of target cell ligand expression, care must be taken in comparing across cell lines, but can easily be done for the same cell line under different culture conditions. Indeed, the NK-92 cells were significantly more cytotoxic toward A549 (Figure 7A) and H1299 (Figure 7B) cells in 2D cultures than in the 3D tumor models. With increased E:T cell ratio, thus increased NK-92 cell number, there was increased cancer cell killing in both 2D and 3D, thereby supporting the idea that greater NK cell presence in the tumor will improve tumor lysis. Surprisingly, NK-92 cell mediated cytotoxicity was greater against the H1299 cells than the A549 cells in 2D and 3D, which contrasts the infiltration data (Figure 6) showing greater colocalization of NK-92 cells with A549 cells in early stage models. This may suggest that, despite greater infiltration, the killing efficiency upon contact with A549 cells is lower than that with H1299, due to differences in HLA molecule expression.[77] However, repeating the 3D killing assay with the late stage models with the same number of NK-92 cells (50,000 cells), no cytotoxicity was detected for

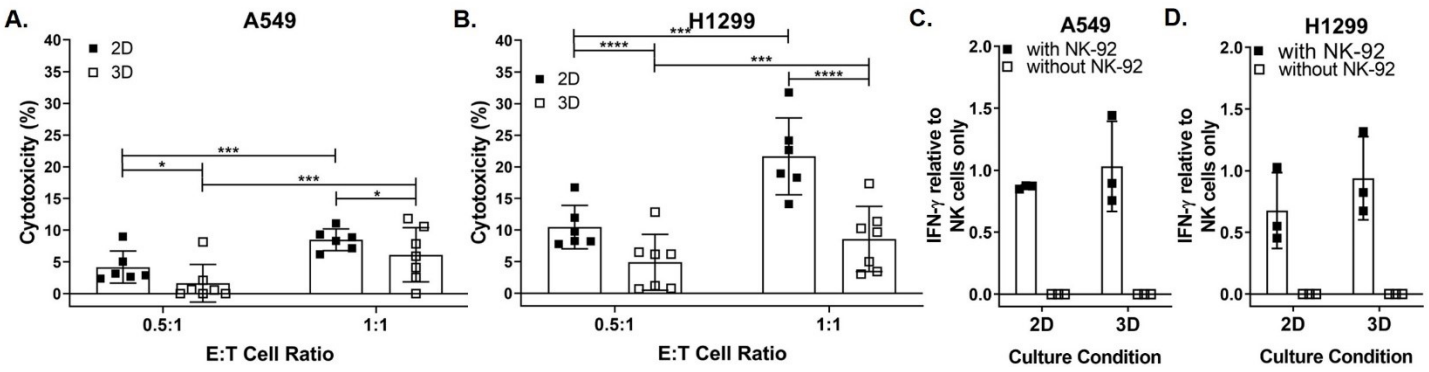

Figure 7. NK-92 cell function during incubation with cancer cells in 2D and 3D cultures. NK-92 cell mediated cytotoxicity to (**A**) A549 and (**B**) H1299 cancer cells cultured in 2D monolayer and early stage 3D tumor models, at E:T cell ratios of 0.5:1 and 1:1 (n=7). Production of IFN-γ by the NK-92 cells incubated with (**C**) A549 and (**D**) H1299 cancer cells cultured in 2D monolayer and early stage 3D tumor models, at an E:T cell ratio of 0.5:1 (n=3). For comparison across groups, *** denotes $P \leq 0.001$, and **** denotes $P \leq 0.0001$.

either the A549 or H1299 tumor models (A549 -9.6±2.1%, H1299 -0.3±5.5%; E:T cell ratio cannot be accurately computed for the late stage models), thereby corroborating the infiltration results.

Further assessment of NK-92 cell function was conducted based on the production of a key inflammatory cytokine, IFN-γ, in response to cancer cells in 2D monolayer culture and 3D early stage tumor models. It is important to note that NK-92 cells require IL-2 for survival, and therefore produce IFN-γ as well as other inflammatory molecules at baseline. Consequently, the functional response of NK-92 cells to the cancer cells was noted by their change in the production of cytokines and chemokines relative to baseline NK-92 cells, as well as across culture conditions. Interestingly, there was no difference in the amount of IFN-γ produced by the NK-92 cells incubated with the 2D or 3D culture of the A549 (Figure 7C) or H1299 (Figure 7D) cells, and the level of IFN-γ produced by NK-92 cells incubated with all groups was comparable to baseline NK-92 cells. Furthermore, there was no difference in the amount of IFN-γ produced by the NK-92 cells incubated with the different cell lines, in either culture condition.

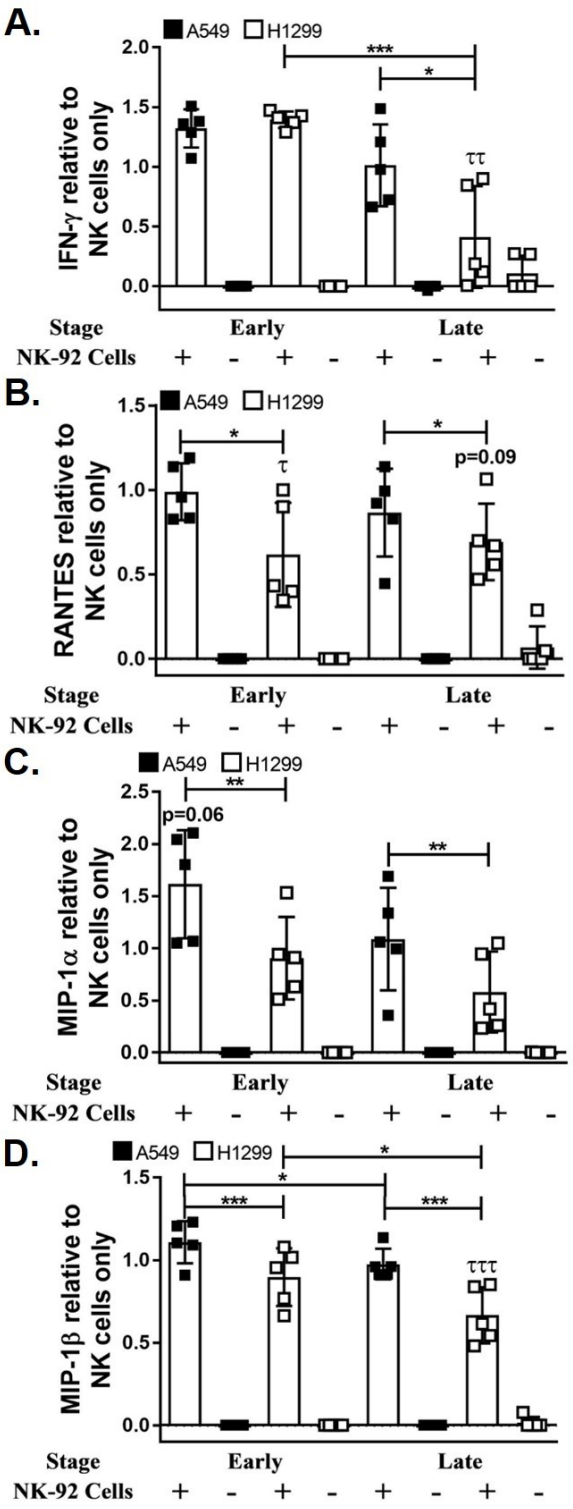

A key feature of the tumor models is the ability to culture cells for extended periods of time, which allows for studying NK cell-cancer cell interactions with evolving tumor microenvironments. As mentioned above, NK-92 cell mediated cytotoxicity was reduced in the late stage models relative to early stages. Similarly, the production of soluble inflammatory signals also changed with stage and cancer cell type. The NK-92 cells incubated with both early stage models and the late stage A549 model produced levels of IFN-γ comparable to baseline NK-92 cells (Figure 8A). However, the NK-92 cells incubated with the late stage H1299 tumor model decreased their production of IFN-γ by 2.4-fold compared to baseline NK-92 cells. Furthermore, the NK-92 cells had a 3.4- and 2.5-fold decrease in the production of IFN-γ when incubated with the late stage H1299 tumor model, compared with

Figure 8. Cytokine and chemokine production by NK-92 cells incubated with the tumor models. ELISAs were used to determine the amount of (**A**) IFN-γ, (**B**) RANTES, (**C**) MIP-1α, and (**D**) MIP-1β produced by NK-92 cells incubated with the A549 and H1299 tumor models at the early and late stage (n=5). For comparison across groups, * denotes $P \leq 0.05$, ** denotes $P \leq 0.01$, and *** denotes $P \leq 0.001$. For comparison to baseline, τ denotes $P \leq 0.05$, ττ denotes $P \leq 0.01$, and τττ denotes $P \leq 0.001$.

the early stage H1299 and late stage A549 models. Out of all the co-culture systems, only a significant reduction in IFN-γ production was observed by the NK-92 cells incubated with the late stage H1299 tumor model, which demonstrates the need to study NK cell function in response to cancer cells at different developmental stages, which is not supported by current 2D systems.

Upon activation, NK cells produce many chemokines that amplify the recruitment of more NK cells and other immune cells to the site of inflammation, including RANTES, MIP-1α, and MIP-1β, which were studied here. While the NK-92 cells incubated with the A549 tumor models produced comparable levels of RANTES to baseline, the NK-92 cells decreased their production by 38% during incubation with the early stage H1299 tumor model compared to baseline NK-92 cells (Figure 8B). Relative to the NK-92 cells incubated with the A549 models, the NK-92 cells incubated with the H1299 tumor models decreased their production of RANTES by 39% and 25% at both early and late stages, respectively. Similarly, relative to the NK-92 cells incubated with the A549 models, the cells incubated with the H1299 models decreased their production of MIP-1α by 44% and 45%, respectively (Figure 8C). However, the production of RANTES or MIP-1α by the NK-92 cells incubated with the tumor models did not depend on the stage of the models. In the case of MIP-1β, the NK-92 cells incubated with early stage models and the late stage A549 model produced comparable amounts to baseline NK-92 cells, the cells incubated with the late stage H1299 models had a decrease of 46% in the production, relative to baseline NK-92 cells (Figure 8D). In comparing across the stage and cell type, statistically significant, albeit modest, differences in the production of MIP-1β by NK-92 cells was observed. The NK-92 cells incubated with early and late stage H1299 tumor models produced 24% and 47% less MIP-1β than the NK-92 cells incubated with the corresponding A549 models.

Additionally, the NK-92 cells incubated with each of the late stage models produced less MIP-1β than their corresponding early stage tumor models, by 14% and 35% for A549 and H1299, respectively. Overall, these data demonstrate differences in NK-92 cell function in response to different cancer cell types and stages of 3D growth.

MMP and Integrin Gene Expression in NK-92 Cell in Response to Tumor Models

Since the different tumor models inhibited NK-92 cell infiltration to varying degrees, we proceeded to determine if these findings corresponded to differences in the expression of genes related to cell migration and adhesion. While the gene expression of MMP2 and MMP13 in NK-

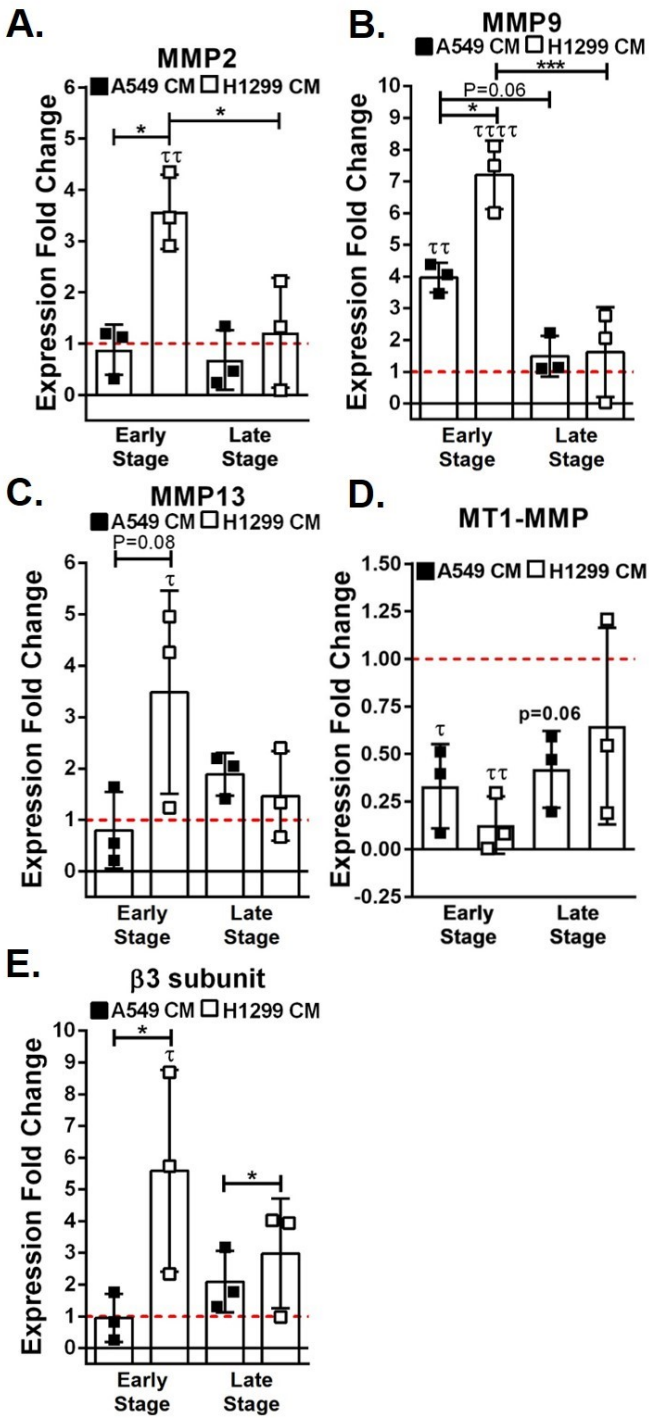

Figure 9. Gene expression profiles of NK-92 cells incubated with conditioned media (CM) from the tumor models. Quantitative RT-PCR was performed to determine the expression fold change of (**A**) soluble matrix metalloproteinase 2 (MMP2), (**B**) MMP9, (**C**) MMP13, (**D**) MT1-MMP, (**E**) β3 integrin subunit from the RNA of NK-92 cells treated with CM from the various tumor models (n=3). Fold change compared to NK-92 cells in fresh coculture media, and the baseline is indicated by the red dotted line. For comparisons across groups, * denotes $P \leq 0.05$ and *** denotes $P \leq 0.001$. For comparison to baseline, τ denotes $P \leq 0.05$, ττ denotes $P \leq 0.01$, and τττ denotes $P \leq 0.0001$.

92 cells treated with conditioned media (CM) from the early stage A549 model was similar to baseline NK-92 cells (Figure 9A and 9C), the gene expression of MMP9 was increased 4-fold compared to baseline (Figure 9B). Conversely, in response to the CM from the early stage H1299 models, NK-92 cell gene expression of MMP2, MMP9, and MMP13 increased by 3.6-, 7.2, and 3.5-fold, respectively, relative to baseline NK-92 cells. The expression of the same MMP genes in NK-92 cells exposed to CM from both A549 and H1299 late stage models was comparable to baseline levels. In comparing the MMP gene expression profiles in NK-92 cells across the treatment with CM from the tumor models, differences were observed with respect to cell type and stage of growth. Relative to NK-92 cells treated with CM from early stage H1299 models, the gene expression of MMP2 and MMP9 by NK-92 cells significantly decreased, by 2.9- and 4.4-fold, respectively, when treated with CM from the late stage H1299 model. Between the A549 models, there was only a trend of decreased MMP9 gene expression in NK-92 cells treated with CM from the late stage model relative to CM from the early stage model ($p=0.06$). Surprisingly, the NK-92 cells incubated with CM from the early stage A549 model had lower gene expression of MMP2 and MMP9 than the NK-92 cells incubated with CM from the early stage H1299 model. A similar, though not statistically significant trend ($p=0.08$), was observed with MMP13 gene expression. These findings demonstrate that the soluble factors produced by the early stage models, especially early stage H1299, led to increased MMP gene expression in NK-92 cells, but those secreted by the late stage models did not have as great as an effect on MMP gene expression. Gene expression of MMP1 in NK-92 cells exposed to CM from the tumor models was comparable to baseline NK-92 cells and not statistically different from each other (Figure S11A). Focusing on the gene expression of membrane-bound MMPs, the expression of MT1-MMP by NK-92 cells was reduced by 3- and 7.8-fold in NK-92 cells exposed

to CM from early stage A549 and H1299 tumor models, respectively, relative to baseline (Figure 9D). This trend in downregulated MT1-MMP gene expression was also observed by NK-92 cells treated with the CM from the late stage A549 model ($p=0.06$). Gene expression of three other membrane-bound MMPs, MT2-, MT3-, and MT6-MMP in NK-92 cells exposed to CM from tumor models were comparable to baseline NK-92 cells, and not statistically different from each other (Figure S11B, S11C, and S11D). These findings demonstrate the soluble factors from the early stage tumor models, and to some extent the late stage A549 model, inhibited the gene expression of MT1-MMP.

Lastly, genes for integrin subunits relevant to the adhesion sites in the hydrogel were analyzed in NK-92 cells exposed to CM from the tumor models. The gene expression of the integrin subunits was generally similar to baseline NK-92 cells (Figure S11E and S11F), except for the expression of the β3 integrin subunit (Figure 9E). The expression of the β3 integrin subunit gene was increased in NK-92 cells by 5.6-fold when exposed to CM from the early stage H1299 model relative to baseline NK-92 cells. As such, the gene expression of the β3 subunit decreased by 5.9-fold in the NK-92 cells exposed to CM from the early stage A549 tumor model relative to CM from the early stage H1299 model. A similar difference in the expression of the β3 subunit gene between NK-92 cells exposed to CM from the late stage A549 and H1299 models was also observed. These findings demonstrated the integrin subunit genes tested were not highly influenced by the soluble factors excreted by the tumor models, expect for the β3 expression, which was most sensitive to the factors by the H1299 models.

Application of Hydrogel System to Probe the Effects of Cytokines on NK-92 Cell Migration

To further probe the role of soluble cues on NK-92 cell migration within the 3D hydrogels and tumor models, we focused on TGF-β, since this cytokine was produced to the greatest extent among the cytokines and chemokines studied and showed differences across both cell type and stage (Figure 5A). We first investigated the effect of incorporating TGF-β1 into the SDF-1α point source on NK-92 cell migration into the MMP degradable hydrogels with 5 mM RGD. The amount of infiltrating NK-92 cells into the hydrogels with TGF-β1 and SDF-1α decreased by 42% relative to the amount in the hydrogels containing only SDF-1α (Figure 10A). Furthermore, in hydrogels with a point source of TGF-β1 and SDF-1α, the cells maximum migration distance decreased by 200 μm relative to the distance in gels with only SDF-1α, corresponding to distances of 1475 μm and 1675 μm, respectively (Figure 10B). Interestingly, the amount of infiltrating NK-92 cells was not increased, but their maximum migration distance increased by 200 μm in the hydrogel with SDF-1α added to a TGF-β1 point source, relative to the amount in the hydrogel with a TGF-β1 point source alone. Still, for hydrogels with TGF-β1 alone or in combination with SDF-1α, the majority of infiltrating NK-92 cells were within 125

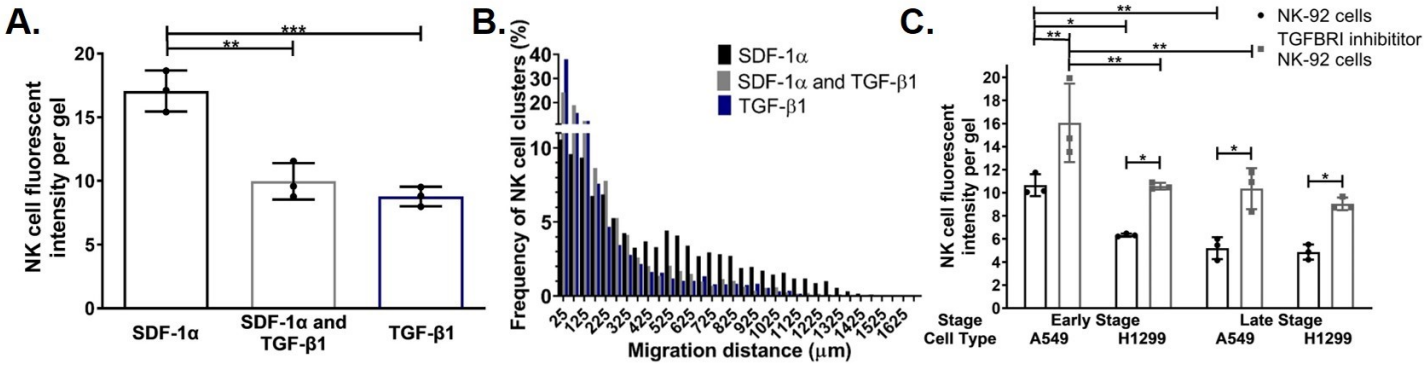

Figure 10. Effect of TGF-β on NK-92 cell migration into hydrogels and infiltration into tumor models. (**A**) Total fluorescent intensity of NK-92 cells and (**B**) frequency of NK-92 cell clusters at increasing migration distances in the PEG-DA, PEG-dMMP-PEG, and 5 mM PEG-RGD hydrogel with a SDF-1α, SDF-1α and TGF-β1, or TGF-β1 point source (n=3 gels). (**C**) Quantification of fluorescent intensity of NK-92 cells in the A549 and H1299 tumor models compared to TGFBRI inhibitor treated NK-92 cells in the tumor models (n=3 gels). For (A) and (C), * denotes $P \leq 0.05$, ** denotes $P \leq 0.01$, and *** denotes $P \leq 0.001$.

μm from the edge of the gel.

To evaluate the effect of TGF-β on NK-92 cell migration into the tumor models, NK-92 cell migration was assessed after treatment with the TGF-β receptor I (TGFBRI) inhibitor LY2157299. Upon treatment with the TGFBRI inhibitor, the amount of NK-92 cells infiltrating into all the tumor models significantly increased compared to the amount in the respective model with untreated NK-92 cells (Figure 10C). Furthermore, for both untreated and TGFBRI inhibitor treated NK-92 cells, the amount of infiltrated NK cells was significantly greater in the early stage A549 tumor model, relative to that in the early stage H1299 tumor model and late stage A549 tumor model, as observed in Figure 6C. Interestingly, the amount of NK-92 cells in the early stage H1299 and both late stage models after TGFBRI inhibitor treatment were comparable to the amount of infiltrated untreated NK-92 cells in the early stage A549 tumor model (all $p>0.999$).

Discussion

PEG-based hydrogels have been used to mimic extracellular matrix environments to study *in vitro* vascular networks,[40] human organoid generation,[78] and 3D tumor biology.[25,26,39,41] Notable advantages of PEG-based hydrogels include the ability to independently control the biochemical and mechanical properties, and the relative ease of incorporating extracellular matrix (ECM) components.[25,39] To our knowledge, this was the first study that employed PEG-based hydrogels to study NK cell migration and cancer cell-NK cell interactions. While the previous studies utilizing tumor spheroids[32–34] and Matrigel assays[35] provide information about which factors may influence NK cell migration and NK cell-cancer cell interactions, the experimental systems do not allow for controllable, independent manipulation of biochemical and mechanical properties, which makes delineating their contributions to NK cell migration

difficult. Here, we set out to (i) establish a synthetic PEG-based hydrogel system to investigate biochemical properties desirable for NK cell migration, (ii) characterize the production of soluble immunomodulatory molecules by cancer cells cultured in the PEG-based hydrogels over time, and (iii) study NK cell infiltration and NK cell-cancer cell interactions in a 3D microenvironment. Our results demonstrate the utility and feasibility of our system in elucidating soluble and insoluble cues that affect NK cell infiltration and function.

Hydrogels were synthesized with components important for NK cell migration, based on *in vitro* and *in vivo* studies to date, followed by systematic studies to determine how these components did, in fact, contribute to NK cell migration. Studies in 2D and 3D Matrigel assays suggested that MMP expression and matrix interaction through integrins influence NK cell migration,[36,37,46] thus the PEG-based hydrogels were engineered to incorporate non-specific MMP cleavable sites and RGD cell adhesion sites. For this study, the cRGD sequence which mimics the binding sites on vitronectin was utilized. Vitronectin is highly expressed in solid tumors, including lung tumors.[79–81] Additionally, in an *in vivo* study of hepatic tumors, the presence of vitronectin corresponded to greater presence and retention of NK cells by histopathology.[82] Based on this finding, and the expression of integrins for vitronectin ($\alpha_v\beta_3$ and $\alpha_v\beta_5$) by NK cells,[44–46] the inclusion of this RGD sequence was a rational starting point for this hydrogel platform development study. Functionalizing the hydrogel with the selected peptides was shown to be important for supporting NK-92 cell migration toward a chemoattractant point source. SDF-1α was selected as the chemoattractant in this model, as it plays a role in stimulating migration of T, B, and NK cells to sites of inflammation and malignancies[36,83,84] at concentrations ranging from 450 pg/mL to 200 ng/mL *in vivo*.[85–87] Thus the 1 ng/mL of SDF-1α released from the hydrogels was in the physiological range, sufficient to promote migration.

Though the point source was not optimized in this study, the 100 ng of SDF-1α encapsulated in the hydrogel was successful in generating a chemokine gradient conducive to NK-92 cell migration. It is possible that the phenomena observed here are dependent on our selected ECM molecules and substrates, and may not fully represent NK cell migration mechanisms in tumors, which comprise numerous ECM molecules and potential adhesion sites. While this matter arises here and with the majority of PEG-based hydrogels in literature, this model does provide a foundation for a reductionist *in vitro* approach to manipulating various ECM components of the tumor microenvironment to elucidate the tri-part interactions of the ECM, NK cells, and cancer cells that are difficult to interrogate *in vivo.*

The tunable properties of PEG hydrogels enabled the investigation of the roles of MMPs and integrins in NK-92 cell migration in a 3D system, while holding the mechanical properties and crosslinking density constant. The importance of MMPs in NK-92 cell migration was corroborated by migration studies in non-degradable hydrogels and in studies using an MMP inhibitor, which reduced NK-92 cell migration towards the SDF-1α point source. Furthermore, the importance of adhesion sites for NK-92 cell migration was demonstrated by the decreased NK-92 cell migration into the hydrogels with lower concentrations of RGD, those with control RAD, and in studies with soluble RGD in the media. This implies that the ECM serves as a substrate for NK cell migration, and its density and/or composition may, therefore, influence NK cell infiltration into tumors. Indeed, our findings suggest that the NK-92 cells predominately utilized mesenchymal migration, an integrin and protease dependent mode of migration,[88,89] in the PEG-based hydrogels. Yet, the observed migration in non-degradable and non-adhesive hydrogels and in inhibitor and integrin blocking studies may indicate the cells might also exhibit some level of amoeboid-like migration. This mode of migration is a protease and integrin

independent, and utilized by other highly motile immune cells in 3D ECMs.[88,89] The extent to which we can understand immune cell infiltration has implications on treatment strategies that consider the entire tumor microenvironment. For example, MMP inhibitors aimed at blocking the invasive and metastatic cascade in cancer cells could inadvertently prevent much needed immune cell migration. The chemoattracting PEG-based hydrogel system presented here provides a framework to interrogate NK cell migration mechanisms in a 3D context, in response to different extracellular cues.

In this study, two NSCLC cell lines were used to evaluate how the metastatic potential of cells influences stress ligand expression and production of soluble immunomodulatory molecules. As with other reported PEG-based hydrogels,[25,26,39,41] the cancer cells remained viable, proliferated, and formed cell clusters over time in culture in the 3D hydrogel. A key distinction of our study was the focus on characterizing certain soluble immunomodulatory factors of the cancer cells in the hydrogels and comparing these factors to 2D culture of the cells, which had not been previously reported. Similar to *in vivo* findings for metastatic tumors,[90–92] the metastatic H1299 tumor models exhibited stress-ligand downregulation and an inhibitory profile of soluble immunomodulatory molecules than the non-metastatic A549 tumor models; this was demonstrated by downregulated stress ligand ULBP1 expression in this cell line,[93] increased MICA shedding, increased TGF-β production, and decreased MCP-1 production. Malignant cells with increased expression of stress-induced ligands are more readily recognized as abnormal by NK cells through the NKG2D receptor, which initiates lysis of the target cells, while cells that downregulate stress ligand expression are more likely to evade immune detection.[1,2] Furthermore, shedding of stress ligands impairs the expression of NKG2D on NK cells,[94] and decreases NK cell infiltration into tumors.[95] However, the fate of the target cell still relies

heavily on the balance of all activating and inhibitory signals the NK cell receives. The H1299 tumor models produced more TGF-β than the A549 models, which in NSCLC patients promotes tumor growth, signifies late stage disease and metastasis, and correlates with a poor prognosis.[96–98] TGF-β has a direct suppressive effect on NK cells through many mechanisms, such as impairing cytolysis and perforin polarization, and decreasing cytokine and chemokine production.[14,99] Conversely, MCP-1 is a chemokine involved in recruiting immune cells to the tumor site *in vivo*;[100] therefore, the decreased production of MCP-1 by the H1299 tumor models suggests a possible mechanism to evade immune cell infiltration and detection. Tumors also produce chemokines to recruit leukocytes for polarization to an immune tolerant and tumor-supportive state, which may explain the increased production of CXC3L1 by the late stage H1299 tumor model. This finding is consistent with clinical reports noting increased CXC3L1 levels with increased tumor pathological status.[101,102] Overall, the data predominantly suggest the soluble immunomodulatory factors produced by the more metastatic cell line, H1299, have an increased ability to inhibit NK cell migration and function than the non-metastatic cell line, A549.

The production of the soluble immunomodulatory molecules changed with time in culture in the 3D tumor models, in a manner similar to tumor progression in patients.[90,91,103] Although the early and late stage tumor models may not necessarily mimic early and advanced tumors *in vivo,* the results from this study indicate these stages were a reasonable approximation of the evolution of the tumor microenvironment. For example, the late stage tumor models showed higher TGF-β production than the respective early stage models, which correlated with decreased NK-92 cell infiltration and function. Furthermore, the A549 tumor models became stiffer over time, which is a characteristic of *in vivo* tumor progression.[103] This study did not

characterize the ECM produced by the cancer cells over time, so it remains unknown if the increase in stiffness was due ECM deposition or to the cancer cells themselves becoming stiffer. These data show that the tumor models cultured for greater periods of time have an increased ability to inhibit NK cell migration and function, relative to tumor models cultured for shorter periods of time. In this study, the tumor microenvironment was largely influenced by the characteristics of the cancer cells; however, given the tunability of PEG-based systems, this study provides a foundation to manipulate numerous biochemical and mechanical cues to systematically interrogate the factors that contribute to suppressive tumor networks. Likewise, stromal cells, like cancer associated fibroblasts, play a large role in tumor ECM deposition, immunosuppression, and metastasis[104] – this hydrogel system allows for incorporation of these, and other cells, to build more complex and biomimetic tumor models.

Patients with advanced solid tumors have lower numbers of tumor infiltrating NK cells,[5,6] which is attributed to the establishment of an immunosuppressive environment within tumors. In our studies, the different production profiles of soluble immunomodulatory molecules by the tumor models led to distinct NK-92 cell-cancer cell interactions, which resembled findings from patient tumors. The tumor models that shed more MICA, produced more TGF-β and less MCP-1 corresponded to decreased NK-92 cell infiltration and colocalization with cancer cells. A reduction in NK-92 cell migration was observed even in the presence of increasing CXC3L1, as observed in the late stage H1299 model, suggesting the effects of the chemokine were likely outweighed by a concomitant increase in TGF-β. Indeed, in our studies TGF-β emerged as playing a dominate role in NK cell infiltration, as the H1299 models and late stage models produced more TGF-β, and had less NK-92 cell infiltration, than the A549 models and early stage models, respectively. Moreover, inhibiting TGF-β signaling in NK-92 cells increased their

migration into all tumor models, and restored NK-92 cell migration into H1299 models and late stage models to levels comparable to control NK-92 cells in A549 models and early stage models, respectively. It is well known that TGF-β acts to suppress NK cell cytotoxicity and cytokine/chemokine production[14,99], but its role in NK cell migration is not well understood. Systemic inhibition of TGF-β in colon[105] and breast[106] cancer murine models led to increased presence of NK cells in tumors, however, given the role of TGF-β on many tumorigenic processes, the effects of TGF-β inhibition on specific cells types in these models could not be delineated. This underscores the advantages 3D tumor models in which we can test the perturbation of specific signals, both soluble and insoluble, on NK cell migration. In addition to the production of soluble factors, the physical properties of tumors may impact immune cell infiltration. Cell migratory behavior and mechanisms can differ based on substrate stiffness,[88,107] which may have contributed to the differences between the NK-92 cell migration in the late stage A549 tumor model and the early stage A549 model, and also the late stage H1299 model. However, the role of matrix stiffness on NK cell migration is unknown, and further studies are needed to understand the mechanotransduction mechanisms of NK cells.

Interestingly, though MMPs and integrins were important for NK-92 cell migration, the differences in migration into the hydrogels and tumor models cannot be explained readily by changes in MMP and integrin expression. In studies examining NK-92 cell migration in the hydrogel toward a point source, SDF-1α was required for migration, but did not impact gene expression levels of MMPs or integrins. This could be a consequence of the required IL-2 stimulation, as IL-2 has been shown to increase MMP[37,42,43] and integrin[45,46] expression in primary NK cells and the YT NK cell line. Further evaluation of protein expression, protease activity, and integrin clustering in corroboration with gene expression will be important for

understanding the migratory mechanisms involved. In the conditioned media studies, the expression of soluble MMPs was actually higher in NK-92 cells in response to soluble factors from H1299 models compared to A549 models, which contrasts the migration data. Yet, there was a consistent trend of downregulation of soluble MMPs in NK-92 cells treated with CM from early stage models compared to those treated with CM from late stage models, which could explain the decreased NK-92 cell infiltration the late stage models. The increase in MMP9 expression could suggest a crucial role of this protease in NK cell migration, as primary NK cells in colorectal cancer patients have increased MMP9 protein expression as well.[108] MT1-MMP expression was significantly downregulated in NK-92 cells exposed to the CM from early stage tumor models, which may implicate this as a mechanism to inhibit NK cell migration. Overall, this study provides new insights into how the combination of soluble factors produced by tumors impact the gene expression of MMPs and integrins in NK-92 cells, which has largely been limited to *in vitro* studies with individual cytokines and chemokines, such as IL-2,[37,42,43] IL-18,[109] and SDF-1α.[36]

Conventionally, NK cell based immunotherapies are tested for their cytotoxicity against 2D culture of cancer cells, and then progress to *in vivo* studies[110]. However, in 2D NK cells can readily come in contact with cancer cells for efficient lysis, while i*n vivo* there are numerous barriers for NK cell-cancer cell interaction to occur – this includes survival of NK cells, homing and infiltration into the tumor, and making contact with cancer cells rather than remaining in the stroma.[30,31,110] The use of 3D tumor models to study NK cell-cancer cell interactions may help bridge the gaps between 2D and *in vivo* by creating a biophysical environment mimetic of barriers in *in vivo* tumors. In our study, 2D assays revealed more potent NK cell mediated killing of H1299 cells compared to A549 cells, likely due to differences in ligand profile that

corresponds to activating receptors on the NK-92 cells.[77] However, the 3D H1299 tumor models experienced relatively lower NK cell infiltration and activating cytokine/chemokine production. As such, we posit that distinct mechanisms may be involved in regulating NK cell migration and NK cell-mediated cytotoxicity. While their cytotoxic functions upon cell contact rely on a balance of signals received through inhibitory and activating cell surface receptors, NK cell migration may be regulated primarily by the balance of tumor-derived chemoattractants and chemorepellants in addition to the biophysical properties of the tumor environment. Effective overall tumor lysis requires both efficient infiltration into the tumor microenvironment as well as recognition of cancer cells upon cell contact. Therefore, the evaluation of both NK cell migration and function in 3D co-cultures may provide a more comprehensive understanding of the factors regulating NK cell-cancer cell interactions.

The differences in migration of the NK-92 cells in the tumor models coincided with changes in cytokine and chemokine production. The NK-92 cells generally produced less IFN-γ, RANTES, MIP-1α, and MIP-1β during incubation with the models with increased MICA shedding, increased production of TGF-β, and decreased production of MCP-1. NK cells are early and potent producers of IFN-γ, which has an anti-proliferative and anti-metabolic effect on many types of tumor cells, promotes cancer cell apoptosis,[1,2,111] and increases tumor recognition by the innate and adaptive immune systems.[111] RANTES is produced by NK cells to attract other immune cells to the target site to mount a robust immune response to the malignancy.[112–114] MIP-1α/β attracts immune cells to the site of inflammation, increases NK cell cytolytic activity, and helps with the release of granzymes.[115] Altogether, the differences in the production of these cytokines and chemokines between cell type and stage, suggest reduced function of NK-92 cells incubated with the more metastatic H1299 models compared to non-metastatic A549 and in late

stage models compared to early stage. The 3D tumor models in this study allow for studying how metastatic potential and stage of growth influences NK cell infiltration, co-localization with cancer cells, and functional activity.

Overcoming the poor infiltration of NK cells into solid tumors is critical to unleashing their therapeutic potential. However, most experimental therapies for cytotoxic immune cell-cancer cell interactions, including NK cells, focus primarily on cytotoxic mechanisms rather than migration mechanisms.[24] The tumor models developed in this study were able to recapitulate some of the complex mechanisms tumors employ to suppress NK cell function and migration, which were dependent on metastatic potential and time in culture. Since studies rarely examine how the duration of cell/tumor growth impacts disease mechanisms and/or therapeutic efficacy,[116] the information found from 'early' and 'late' stage tumor models may help elucidate the mechanisms responsible for the vastly different outcomes of therapies on early versus late stage patient tumors.[10,117] Importantly, this study established a tunable *in vitro* system to interrogate the mechanisms of NK cell infiltration and function in the solid tumor microenvironment, thereby providing a foundation for investigation into the cell-cell and cell-ECM cues within solid tumors that impact NK cell migration and function. Such models may help bridge the gap between conventional 2D assays and *in vivo* animal and human data, and may be useful for identifying new targets for NK cell based immunotherapies, as well as testing their effectiveness.

Acknowledgments

This work was supported by grant support from the Florida Department of Health through the James and Ester King Biomedical Research Program (Award #6JK01) and the National Science Foundation (NSF) Division of Chemical, Bioengineering, Environmental and Transport Systems

(CBET) Faculty Early Career Development (CAREER) Program (Award #1845728). Sheng Wei (previously of Moffitt Cancer Center) worked on an earlier version of this paper and is thanked for his contribution. The authors would like to acknowledge Jahnelle Jordan for assistance with running ELISAs and Thu Le Trinh for assistance with the NK-92 cell culture and use. The authors would also like to acknowledge The University of Florida Health Cancer Center Division of Quantitative Sciences & Biostatistics Shared Resources for assistance with statistical methods for analyzing our data.

ASSOCIATED CONTENT

Supporting Information

The following file is available free of charge:

Supporting Information for Publicantion.pdf

Supplementary Methods, Supplementary Tables of the MMP, integrin, soluble immunomodulatory molecules, and GAPDH primers used for quantitative RT-PCR, and the various chemokines and cytokines tested by ELISAs. Supplementary Scheme for the NK-92 cell migration into the hydrogels with SDF-1α point source. Supplementary Figures of NK-92 cell migration into hydrogels with and without the SDF-1α point source, Three-dimensional renderings from confocal microscopy of the NK-92 cell migration into the various hydrogel compositions, MMP and integrin gene expression in NK-92 after treatment with SDF-1α, Brightfield images and Live/Dead images of the tumor models immediately following cancer cell encapsulation, Cytokines, chemokines, and MICA production by the cancer cells cultured in a 2D monolayer and the 3D tumor models, Gene expression of soluble immunomodulatory molecules in A549 and H1299 xenograft tumors, MICA/B and ULBP1 immunofluorescent staining of late stage tumor models, Cytokines, chemokines, and MICA production by the cancer

cells culture in the 3D tumor models normalized to DNA content, Control fluorescently labeled tumor models without NK-92 cell incubation, NK-92 cell migration into early stage models at 10 million cells/mL and 20 million cells/mL, Gene expression of other MMP's and integrin subunits in NK-92 cells treated with the CM from the different tumor models.

References

(1) Moretta, L.; Montaldo, E.; Vacca, P.; Del Zotto, G.; Moretta, F.; Merli, P.; Locatelli, F.; Mingari, M. C. Human Natural Killer Cells: Origin, Receptors, Function, and Clinical Applications. *Int. Arch. Allergy Immunol.* **2014**, *164* (4), 253–264. https://doi.org/10.1159/000365632.

(2) Sabry, M.; Lowdell, M. W. Tumor-Primed NK Cells: Waiting for the Green Light. *Front. Immunol.* **2013**, *4* (NOV), 1–7. https://doi.org/10.3389/fimmu.2013.00408.

(3) Orange, J. S. Natural Killer Cell Deficiency. *J. Allergy Clin. Immunol.* **2013**, *132* (3), 515–525. https://doi.org/10.1016/j.jaci.2013.07.020.

(4) Mace, E. M.; Orange, J. S. Genetic Causes of Human NK Cell Deficiency and Their Effect on NK Cell Subsets. *Front. Immunol.* **2016**, *7*, 545. https://doi.org/10.3389/fimmu.2016.00545.

(5) Villegas, F. R.; Coca, S.; Villarrubia, V. G.; Jiménez, R.; Chillón, M. J.; Jareño, J.; Zuil, M.; Callol, L. Prognostic Significance of Tumor Infiltrating Natural Killer Cells Subset CD57 in Patients with Squamous Cell Lung Cancer. *Lung Cancer* **2002**, *35* (1), 23–28. https://doi.org/10.1016/S0169-5002(01)00292-6.

(6) Burke, Shannon; Lakshmikanth, Tadepally; Colucci, Francesco; Carbone, E. New Views on Natural Killer Cell-Based Immunotherapy for Melanoma Treatment. *Trends Immunol.* **2010**, *31* (9), 339–345. https://doi.org/10.1016/J.IT.2010.06.003.

(7) Williams, B. A.; Law, A. D.; Routy, B.; denHollander, N.; Gupta, V.; Wang, X.-H.; Chaboureau, A.; Viswanathan, S.; Keating, A.; Williams, B. A.; Law, A. D.; Routy, B.; denHollander, N.; Gupta, V.; Wang, X.-H.; Chaboureau, A.; Viswanathan, S.; Keating, A. A Phase I Trial of NK-92 Cells for Refractory Hematological Malignancies Relapsing after Autologous Hematopoietic Cell Transplantation Shows Safety and Evidence of Efficacy. *Oncotarget* **2017**, *8* (51), 89256–89268. https://doi.org/10.18632/oncotarget.19204.

(8) Curti, A.; Ruggeri, L.; D'Addio, A.; Bontadini, A.; Dan, E.; Motta, M. R.; Trabanelli, S.; Giudice, V.; Urbani, E.; Martinelli, G.; Paolini, S.; Fruet, F.; Isidori, A.; Parisi, S.; Bandini, G.; Baccarani, M.; Velardi, A.; Lemoli, R. M. Successful Transfer of Alloreactive Haploidentical KIR Ligand-Mismatched Natural Killer Cells after Infusion in Elderly High Risk Acute Myeloid Leukemia Patients. *Blood* **2011**, *118* (12), 3273–3279. https://doi.org/10.1182/blood-2011-01-329508.

(9) Miller, J. S.; Soignier, Y.; Panoskaltsis-Mortari, A.; McNearney, S. A.; Yun, G. H.; Fautsch, S. K.; McKenna, D.; Le, C.; Defor, T. E.; Burns, L. J.; Orchard, P. J.; Blazar, B. R.; Wagner, J. E.; Slungaard, A.; Weisdorf, D. J.; Okazaki, I. J.; McGlave, P. B. Successful Adoptive Transfer and in Vivo Expansion of Human Haploidentical NK Cells in Patients with Cancer. *Blood* **2005**, *105* (8), 3051–3057. https://doi.org/10.1182/blood-2004-07-2974.

(10) American Cancer Society. Cancer Facts & Figures 2018. In *Atlanta: American Cancer Society*; 2018.

(11) Parkhurst, M. R.; Riley, J. P.; Dudley, M. E.; Rosenberg, S. A. Adoptive Transfer of Autologous Natural Killer Cells Leads to High Levels of Circulating Natural Killer Cells

but Does Not Mediate Tumor Regression. *Clin. Cancer Res.* **2011**, *17* (19), 6287–6297. https://doi.org/10.1158/1078-0432.CCR-11-1347.

(12) Geller, M. A.; Cooley, S.; Judson, P. L.; Ghebre, R.; Carson, L. F.; Argenta, P. A.; Jonson, A. L.; Panoskaltsis-Mortari, A.; Curtsinger, J.; McKenna, D.; Dusenbery, K.; Bliss, R.; Downs, L. S.; Miller, J. S. A Phase II Study of Allogeneic Natural Killer Cell Therapy to Treat Patients with Recurrent Ovarian and Breast Cancer. *Cytotherapy* **2011**, *13* (1), 98–107. https://doi.org/10.3109/14653249.2010.515582.

(13) Balsamo, M.; Vermi, W.; Parodi, M.; Pietra, G.; Manzini, C.; Queirolo, P.; Lonardi, S.; Augugliaro, R.; Moretta, A.; Facchetti, F.; Moretta, L.; Mingari, M. C.; Vitale, M. Melanoma Cells Become Resistant to NK-Cell-Mediated Killing When Exposed to NK-Cell Numbers Compatible with NK-Cell Infiltration in the Tumor. *Eur. J. Immunol.* **2012**, *42* (7), 1833–1842. https://doi.org/10.1002/eji.201142179.

(14) Donatelli, S. S.; Zhou, J.-M.; Gilvary, D. L.; Eksioglu, E. A.; Chen, X.; Cress, W. D.; Haura, E. B.; Schabath, M. B.; Coppola, D.; Wei, S.; Djeu, J. Y. TGF- -Inducible MicroRNA-183 Silences Tumor-Associated Natural Killer Cells. *Proc. Natl. Acad. Sci.* **2014**, *111* (11), 4203–4208. https://doi.org/10.1073/pnas.1319269111.

(15) Mamessier, E.; Sylvain, A.; Thibult, M.-L.; Houvenaeghel, G.; Jacquemier, J.; Castellano, R.; Gonçalves, A.; André, P.; Romagné, F.; Thibault, G.; Viens, P.; Birnbaum, D.; Bertucci, F.; Moretta, A.; Olive, D. Human Breast Cancer Cells Enhance Self Tolerance by Promoting Evasion from NK Cell Antitumor Immunity. *J. Clin. Invest.* **2011**, *121* (9), 3609–3622. https://doi.org/10.1172/JCI45816.

(16) Sconocchia, G.; Spagnoli, G. C.; Del Principe, D.; Ferrone, S.; Anselmi, M.; Wongsena, W.; Cervelli, V.; Schultz-Thater, E.; Wyler, S.; Carafa, V.; Moch, H.; Terracciano, L.;

Tornillo, L. Defective Infiltration of Natural Killer Cells in MICA/B-Positive Renal Cell Carcinoma Involves Beta(2)-Integrin-Mediated Interaction. *Neoplasia* **2009**, *11* (7), 662–671.

(17) Albertsson, P. A.; Basse, P. H.; Hokland, M.; Goldfarb, R. H.; Nagelkerke, J. F.; Nannmark, U.; Kuppen, P. J. K. NK Cells and the Tumour Microenvironment: Implications for NK-Cell Function and Anti-Tumour Activity. *Trends Immunol.* **2003**, *24* (11), 603–609. https://doi.org/10.1016/J.IT.2003.09.007.

(18) Carrega, P.; Morandi, B.; Costa, R.; Frumento, G.; Forte, G.; Altavilla, G.; Ratto, G. B.; Mingari, M. C.; Moretta, L.; Ferlazzo, G. Natural Killer Cells Infiltrating Human Nonsmall-Cell Lung Cancer Are Enriched in CD56brightCD16− Cells and Display an Impaired Capability to Kill Tumor Cells. *Cancer* **2008**, *112* (4), 863–875. https://doi.org/10.1002/cncr.23239.

(19) Kuppen, P. J. K.; van der Eb, M. M.; Jonges, L. E.; Hagenaars, M.; Hokland, M. E.; Nannmark, U.; Goldfarb, R. H.; Basse, P. H.; Fleuren, G. J.; Hoeben, R. C.; van de Velde, C. J. H. Tumor Structure and Extracellular Matrix as a Possible Barrier for Therapeutic Approaches Using Immune Cells or Adenoviruses in Colorectal Cancer. *Histochem. Cell Biol.* **2001**, *115* (1), 67–72. https://doi.org/10.1007/s004180000224.

(20) Yang, Q.; Hokland, M. E.; Bryant, J. L.; Zhang, Y.; Nannmark, U.; Watkins, S. C.; Goldfarb, R. H.; Herberman, R. B.; Basse, P. H. Tumor-Localization by Adoptively Transferred, Interleukin-2-Activated NK Cells Leads to Destruction of Well-Established Lung Metastases. *Int. J. Cancer* **2003**, *105* (4), 512–519. https://doi.org/10.1002/ijc.11119.

(21) Guillerey, C.; Huntington, N. D.; Smyth, M. J. Targeting Natural Killer Cells in Cancer

Immunotherapy. *Nat. Immunol.* **2016**, *17* (9), 1025–1036. https://doi.org/10.1038/ni.3518.

(22) Vaday, G. G.; Lider, O. Extracellular Matrix Moieties, Cytokines, and Enzymes: Dynamic Effects on Immune Cell Behavior and Inflammation. *J. Leukoc. Biol.* **2000**, *67* (2), 149–159.

(23) Shen, M. J.; Xu, L. J.; Yang, L.; Tsai, Y.; Keng, P. C.; Chen, Y.; Lee, S. O.; Chen, Y.; Shen, M. J.; Xu, L. J.; Yang, L.; Tsai, Y.; Keng, P. C.; Chen, Y.; Lee, S. O.; Chen, Y.; Shen, M. J.; Xu, L. J.; Yang, L.; Tsai, Y.; Keng, P. C.; Chen, Y.; Chen, S. O. L. and Y. Radiation Alters PD-L1/NKG2D Ligand Levels in Lung Cancer Cells and Leads to Immune Escape from NK Cell Cytotoxicity via IL-6-MEK/Erk Signaling Pathway. *Oncotarget* **2017**, *8* (46), 80506–80520. https://doi.org/10.18632/oncotarget.19193.

(24) Hirt, C.; Papadimitropoulos, A.; Mele, V.; Muraro, M. G.; Mengus, C.; Iezzi, G.; Terracciano, L.; Martin, I.; Spagnoli, G. C. In Vitro 3D Models of Tumor-Immune System Interaction. *Adv. Drug Deliv. Rev.* **2014**, *79–80*, 145–154. https://doi.org/10.1016/j.addr.2014.05.003.

(25) Gill, B. J.; Gibbons, D. L.; Roudsari, L. C.; Saik, J. E.; Rizvi, Z. H.; Roybal, J. D.; Kurie, J. M.; West, J. L. A Synthetic Matrix with Independently Tunable Biochemistry and Mechanical Properties to Study Epithelial Morphogenesis and EMT in a Lung Adenocarcinoma Model. *Cancer Res.* **2012**, *72* (22), 6013–6023. https://doi.org/10.1158/0008-5472.CAN-12-0895.

(26) Wang, C.; Tong, X.; Yang, F. Bioengineered 3D Brain Tumor Model To Elucidate the Effects of Matrix Stiffness on Glioblastoma Cell Behavior Using PEG-Based Hydrogels. *Mol. Pharm.* **2014**, *11* (7), 2115–2125.

(27) Lopez-Lastra, S.; Di Santo, J. P. Modeling Natural Killer Cell Targeted Immunotherapies.

Front. Immunol. **2017**, *8*, 370. https://doi.org/10.3389/fimmu.2017.00370.

(28) Cohen, I. J.; Blasberg, R. Impact of the Tumor Microenvironment on Tumor-Infiltrating Lymphocytes: Focus on Breast Cancer. *Breast Cancer (Auckl).* **2017**, *11*, 1178223417731565. https://doi.org/10.1177/1178223417731565.

(29) Uong, T. N. T.; Lee, K.-H.; Ahn, S.-J.; Kim, K. W.; Min, J.-J.; Hyun, H.; Yoon, M. S. Real-Time Tracking of Ex Vivo-Expanded Natural Killer Cells Toward Human Triple-Negative Breast Cancers. *Front. Immunol.* **2018**, *9*, 825. https://doi.org/10.3389/fimmu.2018.00825.

(30) Song, X.; Hong, S.-H.; Kwon, W. T.; Bailey, L. M.; Basse, P.; Bartlett, D. L.; Kwon, Y. T.; Lee, Y. J. Secretory TRAIL-Armed Natural Killer Cell–Based Therapy: *In Vitro* and *In Vivo* Colorectal Peritoneal Carcinomatosis Xenograft. *Mol. Cancer Ther.* **2016**, *15* (7), 1591–1601. https://doi.org/10.1158/1535-7163.MCT-15-0937.

(31) Wennerberg, E.; Kremer, V.; Childs, R.; Lundqvist, A. CXCL10-Induced Migration of Adoptively Transferred Human Natural Killer Cells toward Solid Tumors Causes Regression of Tumor Growth in Vivo. *Cancer Immunol. Immunother.* **2015**, *64* (2), 225–235. https://doi.org/10.1007/s00262-014-1629-5.

(32) Augustine, T. N.; Dix-Peek, T.; Duarte, R.; Candy, G. P. Establishment of a Heterotypic 3D Culture System to Evaluate the Interaction of TREG Lymphocytes and NK Cells with Breast Cancer. *J. Immunol. Methods* **2015**, *426*, 1–13. https://doi.org/10.1016/J.JIM.2015.07.003.

(33) Giannattasio, A.; Weil, S.; Kloess, S.; Ansari, N.; Stelzer, E. H. K.; Cerwenka, A.; Steinle, A.; Koehl, U.; Koch, J. Cytotoxicity and Infiltration of Human NK Cells in in Vivo-like Tumor Spheroids. *BMC Cancer* **2015**, *15* (1), 351. https://doi.org/10.1186/s12885-015-

1321-y.

(34) Lanuza, P. M.; Vigueras, A.; Olivan, S.; Prats, A. C.; Costas, S.; Llamazares, G.; Sanchez-Martinez, D.; Ayuso, J. M.; Fernandez, L.; Ochoa, I.; Pardo, J. Activated Human Primary NK Cells Efficiently Kill Colorectal Cancer Cells in 3D Spheroid Cultures Irrespectively of the Level of PD-L1 Expression. *Oncoimmunology* **2018**, *7* (4). https://doi.org/10.1080/2162402X.2017.1395123.

(35) Johansson, B. R.; Nannmark, U. Ultrastructure of Interactions between Activated Murine Natural Killer Cells and Melanoma Cells in an Extracellular Matrix (Matrigel) Environment. *Nat. Immun.* **1997**, *15* (2–3), 98–106.

(36) Goda, S.; Inoue, H.; Umehara, H.; Miyaji, M.; Nagano, Y.; Harakawa, N.; Imai, H.; Lee, P.; Macarthy, J. B.; Ikeo, T.; Domae, N.; Shimizu, Y.; Iida, J. Matrix Metalloproteinase-1 Produced by Human CXCL12-Stimulated Natural Killer Cells. *Am. J. Pathol.* **2006**, *169* (2), 445–458. https://doi.org/10.2353/ajpath.2006.050676.

(37) Edsparr, K.; Johansson, B. R.; Goldfarb, R. H.; Basse, P. H.; Nannmark, U.; Speetjens, F. M.; Kuppen, P. J. K.; Lennernäs, B.; Albertsson, P. Human NK Cell Lines Migrate Differentially in Vitro Related to Matrix Interaction and MMP Expression. *Immunol. Cell Biol.* **2009**, *87* (6), 489–495. https://doi.org/10.1038/icb.2009.35.

(38) Gu, L.; Mooney, D. J. Biomaterials and Emerging Anticancer Therapeutics: Engineering the Microenvironment. *Nat. Rev. Cancer* **2016**, *16* (1), 56–66. https://doi.org/10.1038/nrc.2015.3.

(39) Lewis, K. J. R.; Hall, J. K.; Kiyotake, E. A.; Christensen, T.; Balasubramaniam, V.; Anseth, K. S. Epithelial-Mesenchymal Crosstalk Influences Cellular Behavior in a 3D Alveolus-Fibroblast Model System. *Biomaterials* **2018**, *155*, 124–134.

https://doi.org/10.1016/j.biomaterials.2017.11.008.

(40) Nguyen, E. H.; Daly, W. T.; Le, N. N. T.; Farnoodian, M.; Belair, D. G.; Schwartz, M. P.; Lebakken, C. S.; Ananiev, G. E.; Saghiri, M. A.; Knudsen, T. B.; Sheibani, N.; Murphy, W. L. Versatile Synthetic Alternatives to Matrigel for Vascular Toxicity Screening and Stem Cell Expansion. *Nat. Biomed. Eng.* **2017**, *1*. https://doi.org/10.1038/s41551-017-0096.

(41) Roudsari, L. C.; Jeffs, S. E.; West, J. L. Lung Adenocarcinoma Cell Responses in a 3D in Vitro Tumor Angiogenesis Model Correlate with Metastatic Capacity. *ACS Biomater. Sci. Eng.* **2017**, *4*, 368–377. https://doi.org/10.1021/acsbiomaterials.7b00011.

(42) Edsparr, K.; Basse, P. H.; Goldfarb, R. H.; Albertsson, P. Matrix Metalloproteinases in Cytotoxic Lymphocytes Impact on Tumour Infiltration and Immunomodulation. *Cancer Microenviron.* **2011**, *4* (3), 351–360. https://doi.org/10.1007/s12307-010-0057-0.

(43) Edsparr, K.; Speetjens, F. M.; Mulder-Stapel, A.; Goldfarb, R. H.; Basse, P. H.; Lennernäs, B.; Kuppen, P. J. K.; Albertsson, P. Effects of IL-2 on MMP Expression in Freshly Isolated Human NK Cells and the IL-2-Independent NK Cell Line YT. *J. Immunother.* **2010**, *33* (5), 475–481. https://doi.org/10.1097/CJI.0b013e3181d372a0.

(44) Rabinowich, H.; Lin, W. C.; Amoscato, A.; Herberman, R. B.; Whiteside, T. L. Expression of Vitronectin Receptor on Human NK Cells and Its Role in Protein Phosphorylation, Cytokine Production, and Cell Proliferation. *J. Immunol.* **1995**, *154* (3), 1124–1135.

(45) Pé Rez-Villar, J. J.; Zapata, J. M.; Melero, I.; Postigo, A.; Sa´, F. S. Expression and Function of a A4/B7 Integrin on Human Natural Killer Cells. *Cell. Immunol.* **1993**, *152* (2), 481–498.

(46) Rabinowich, H.; Herberman, R. B.; Whiteside, T. L. Differential Effects of IL12 and IL2 on Expression and Function of Cellular Adhesion Molecules on Purified Human Natural Killer Cells. *Cell. Immunol.* **1993**, *152* (2), 481–498. https://doi.org/10.1006/CIMM.1993.1306.

(47) Gong, J. H.; Maki, G.; Klingemann, H. G. Characterization of a Human Cell Line (NK-92) with Phenotypical and Functional Characteristics of Activated Natural Killer Cells. *Leukemia* **1994**, *8* (4), 652–658.

(48) Tonn, T.; Becker, S.; Esser, R.; Schwabe, D.; Seifried, E. Cellular Immunotherapy of Malignancies Using the Clonal Natural Killer Cell Line NK-92. *J. Hematother. Stem Cell Res.* **2001**, *10*, 535–544.

(49) Turturro, M. V.; Christenson, M. C.; Larson, J. C.; Young, D. A.; Brey, E. M.; Papavasiliou, G. MMP-Sensitive PEG Diacrylate Hydrogels with Spatial Variations in Matrix Properties Stimulate Directional Vascular Sprout Formation. *PLoS One* **2013**, *8* (3). https://doi.org/10.1371/journal.pone.0058897.

(50) Yang, F.; Williams, C. G.; Wang, D. A.; Lee, H.; Manson, P. N.; Elisseeff, J. The Effect of Incorporating RGD Adhesive Peptide in Polyethylene Glycol Diacrylate Hydrogel on Osteogenesis of Bone Marrow Stromal Cells. *Biomaterials* **2005**, *26* (30), 5991–5998. https://doi.org/10.1016/j.biomaterials.2005.03.018.

(51) Zhu, J.; Tang, C.; Kottke-Marchant, K.; Marchant, R. E. Design and Synthesis of Biomimetic Hydrogel Scaffolds with Controlled Organization of Cyclic RGD Peptides. *Bioconjug. Chem.* **2009**, *20* (2), 333–339. https://doi.org/10.1021/bc800441v.

(52) Mann, B. K.; Gobin, A. S.; Tsai, A. T.; Schmedlen, R. H.; West, J. L. Smooth Muscle Cell Growth in Photopolymerized Hydrogels with Cell Adhesive and Proteolytically

Degradable Domains: Synthetic ECM Analogs for Tissue Engineering. *Biomaterials* **2001**, *22* (22), 3045–3051. https://doi.org/10.1016/S0142-9612(01)00051-5.

(53) Ruoslahti, E. Rgd and Other Recognition Sequences for Integrins. *Annu. Rev. Cell Dev. Biol.* **1996**, *12* (1), 697–715. https://doi.org/10.1146/annurev.cellbio.12.1.697.

(54) Horton, M. A. The Avβ3 Integrin "Vitronectin Receptor." *Int. J. Biochem. Cell Biol.* **1997**, *29* (5), 721–725. https://doi.org/10.1016/S1357-2725(96)00155-0.

(55) Rie Marchi-Artzner, V. Â.; Lorz, B.; Hellerer, U.; Kantlehner, M.; Kessler, H.; Sackmann, E. Selective Adhesion of Endothelial Cells to Artificial Membranes with a Synthetic RGD-Lipopeptide. *Chem. Eur. J* **2001**, *7* (5).

(56) Zuidema, J. M.; Rivet, C. J.; Gilbert, R. J.; Morrison, F. A. A Protocol for Rheological Characterization of Hydrogels for Tissue Engineering Strategies. *J. Biomed. Mater. Res. Part B Appl. Biomater.* **2014**, *102* (5), 1063–1073. https://doi.org/10.1002/jbm.b.33088.

(57) Cornelison, R. C.; Gonzalez-Rothi, E. J.; Porvasnik, S. L.; Wellman, S. M.; Park, J. H.; Fuller, D. D.; Schmidt, C. E. Injectable Hydrogels of Optimized Acellular Nerve for Injection in the Injured Spinal Cord. *Biomed. Mater.* **2018**, *13* (3), 034110. https://doi.org/10.1088/1748-605X/aaab82.

(58) Young, R. J.; Lovell, P. A. *Introduction to Polymers*, Third Edit.; CRC Press: Boca Raton, FL, 1991.

(59) Kloxin, A. M.; Benton, J. A.; Anseth, K. S. In Situ Elasticity Modulation with Dynamic Substrates to Direct Cell Phenotype. *Biomaterials* **2010**, *31* (1), 1–8. https://doi.org/10.1016/j.biomaterials.2009.09.025.

(60) Ma, H.; Killaars, A. R.; DelRio, F. W.; Yang, C.; Anseth, K. S. Myofibroblastic Activation of Valvular Interstitial Cells Is Modulated by Spatial Variations in Matrix

Elasticity and Its Organization. *Biomaterials* **2017**, *131*, 131–144. https://doi.org/10.1016/j.biomaterials.2017.03.040.

(61) Rao, V. V.; Vu, M. K.; Ma, H.; Killaars, A. R.; Anseth, K. S. Rescuing Mesenchymal Stem Cell Regenerative Properties on Hydrogel Substrates Post Serial Expansion. *Bioeng. Transl. Med.* **2019**, *4* (1), 51–60. https://doi.org/10.1002/btm2.10104.

(62) Anseth, K. S.; Bowman, C. N.; Brannon-Peppas, L. Mechanical Properties of Hydrogels and Their Experimental Determination. *Biomaterials* **1996**, *17* (17), 1647–1657. https://doi.org/10.1016/0142-9612(96)87644-7.

(63) Ahearne, M.; Yang, Y.; El Haj, A. J.; Then, K. Y.; Liu, K.-K. Characterizing the Viscoelastic Properties of Thin Hydrogel-Based Constructs for Tissue Engineering Applications. *J. R. Soc. Interface* **2005**, *2* (5), 455–463. https://doi.org/10.1098/rsif.2005.0065.

(64) Schindelin, J.; Arganda-Carreras, I.; Frise, E.; Kaynig, V.; Longair, M.; Pietzsch, T.; Preibisch, S.; Rueden, C.; Saalfeld, S.; Schmid, B.; Tinevez, J.-Y.; White, D. J.; Hartenstein, V.; Eliceiri, K.; Tomancak, P.; Cardona, A. Fiji: An Open-Source Platform for Biological-Image Analysis. *Nat. Methods* **2012**, *9* (7), 676–682. https://doi.org/10.1038/nmeth.2019.

(65) Marinković, A.; Liu, F.; Tschumperlin, D. J. Matrices of Physiologic Stiffness Potently Inactivate Idiopathic Pulmonary Fibrosis Fibroblasts. *Am. J. Respir. Cell Mol. Biol.* **2013**, *48* (4), 422–430. https://doi.org/10.1165/rcmb.2012-0335OC.

(66) White, E. S. Lung Extracellular Matrix and Fibroblast Function. *Ann. Am. Thorac. Soc.* **2015**, *12* (Supplement 1), S30–S33. https://doi.org/10.1513/AnnalsATS.201406-240MG.

(67) Brown, A. C.; Fiore, V. F.; Sulchek, T. A.; Barker, T. H. Physical and Chemical

Microenvironmental Cues Orthogonally Control the Degree and Duration of Fibrosis-Associated Epithelial-to-Mesenchymal Transitions. *J. Pathol.* **2013**, *229* (1), 25–35. https://doi.org/10.1002/path.4114.

(68) Shukla, V. C.; Higuita-Castro, N.; Nana-Sinkam, P.; Ghadiali, S. N. Substrate Stiffness Modulates Lung Cancer Cell Migration but Not Epithelial to Mesenchymal Transition. *J. Biomed. Mater. Res. Part A* **2016**, *104* (5), 1182–1193. https://doi.org/10.1002/jbm.a.35655.

(69) Liu, F.; Tschumperlin, D. J. Micro-Mechanical Characterization of Lung Tissue Using Atomic Force Microscopy. *J. Vis. Exp.* **2011**, No. 54. https://doi.org/10.3791/2911.

(70) Weber, L. M.; Lopez, C. G.; Anseth, K. S. Effects of PEG Hydrogel Crosslinking Density on Protein Diffusion and Encapsulated Islet Survival and Function. *J. Biomed. Mater. Res. A* **2009**, *90* (3), 720–729. https://doi.org/10.1002/jbm.a.32134.

(71) Omidian, H.; Hasherni, S.-A.; Askari, F.; Nafisi, S. *Swelling and Crosslink Density Measurements for Hydrogels*; 1994; Vol. 3.

(72) Canal, T.; Peppas, N. A. Correlation between Mesh Size and Equilibrium Degree of Swelling of Polymeric Networks. *J. Biomed. Mater. Res.* **1989**, *23* (10), 1183–1193. https://doi.org/10.1002/jbm.820231007.

(73) Schweller, R. M.; West, J. L. Encoding Hydrogel Mechanics via Network Cross-Linking Structure. *ACS Biomater. Sci. Eng.* **2015**, *1*, 335–344. https://doi.org/10.1021/acsbiomaterials.5b00064.

(74) Settanni, G.; Zhou, J.; Schmid, F. Interactions between Proteins and Poly(Ethylene-Glycol) Investigated Using Molecular Dynamics Simulations . *IOP Conf. Ser. J. Phys. Conf. Ser.* **2017**, *921*. https://doi.org/10.1088/1742-6596/921/1/012002.

(75) Wu, J.; Zhao, C.; Lin, W.; Hu, R.; Wang, Q.; Chen, H.; Li, L.; Chen, S.; Zheng, J. Binding Characteristics between Polyethylene Glycol (PEG) and Proteins in Aqueous Solution. *J. Mater. Chem. B* **2014**, *2* (20), 2983–2992. https://doi.org/10.1039/c4tb00253a.

(76) Qu, Z.; Sun, F.; Zhou, J.; Li, L.; Shapiro, S. D.; Xiao, G. Interleukin-6 Prevents the Initiation but Enhances the Progression of Lung Cancer. *Cancer Res.* **2015**, *75* (16), 3209–3215. https://doi.org/10.1158/0008-5472.CAN-14-3042.

(77) Klijn, C.; Durinck, S.; Stawiski, E. W.; Haverty, P. M.; Jiang, Z.; Liu, H.; Degenhardt, J.; Mayba, O.; Gnad, F.; Liu, J.; Pau, G.; Reeder, J.; Cao, Y.; Mukhyala, K.; Selvaraj, S. K.; Yu, M.; Zynda, G. J.; Brauer, M. J.; Wu, T. D.; Gentleman, R. C.; Manning, G.; Yauch, R. L.; Bourgon, R.; Stokoe, D.; Modrusan, Z.; Neve, R. M.; De Sauvage, F. J.; Settleman, J.; Seshagiri, S.; Zhang, Z. A Comprehensive Transcriptional Portrait of Human Cancer Cell Lines. *Nat. Biotechnol.* **2015**, *33* (3), 306–312. https://doi.org/10.1038/nbt.3080.

(78) Cruz-Acuña, R.; Quirós, M.; Huang, S.; Siuda, D.; Spence, J. R.; Nusrat, A.; García, A. J. PEG-4MAL Hydrogels for Human Organoid Generation, Culture, and in Vivo Delivery. *Nat. Protoc.* **2018**, *13* (9), 2102–2119. https://doi.org/10.1038/s41596-018-0036-3.

(79) Gladson, C. L.; Cheresh, D. A. Glioblastoma Expression of Vitronectin and the Alpha v Beta 3 Integrin. Adhesion Mechanism for Transformed Glial Cells. *J. Clin. Invest.* **1991**, *88* (6), 1924–1932. https://doi.org/10.1172/JCI115516.

(80) Burgos-Panadero, R.; Noguera, I.; Cañete, A.; Navarro, S.; Noguera, R. Vitronectin as a Molecular Player of the Tumor Microenvironment in Neuroblastoma. *BMC Cancer* **2019**, *19* (1), 479. https://doi.org/10.1186/s12885-019-5693-2.

(81) Böger, C.; Kalthoff, H.; Goodman, S. L.; Behrens, H.-M.; Röcken, C. Integrins and Their Ligands Are Expressed in Non-Small Cell Lung Cancer but Not Correlated with

Parameters of Disease Progression. *Virchows Arch.* **2014**, *464* (1), 69–78. https://doi.org/10.1007/s00428-013-1506-1.

(82) Edwards, S.; Lalor, P. F.; Tuncer, C.; Adams, D. H. Vitronectin in Human Hepatic Tumours Contributes to the Recruitment of Lymphocytes in an AvB3-Independent Manner. *Br. J. Cancer* **2006**, *95* (11), 1545–1554. https://doi.org/10.1038/sj.bjc.6603467.

(83) Kryczek, I.; Frydman, N.; Gaudin, F.; Krzysiek, R.; Fanchin, R.; Emilie, D.; Chouaib, S.; Zou, W.; Machelon, V. The Chemokine SDF-1/CXCL12 Contributes to T Lymphocyte Recruitment in Human Pre-Ovulatory Follicles and Coordinates with Lymphocytes to Increase Granulosa Cell Survival and Embryo Quality. *Am. J. Reprod. Immunol.* **2005**, *54* (5), 270–283. https://doi.org/10.1111/j.1600-0897.2005.00307.x.

(84) de Gorter, D. J. J.; Reijmers, R. M.; Beuling, E. A.; Naber, H. P. H.; Kuil, A.; Kersten, M. J.; Pals, S. T.; Spaargaren, M. The Small GTPase Ral Mediates SDF-1-Induced Migration of B Cells and Multiple Myeloma Cells. *Blood* **2008**, *111* (7), 3364–3372. https://doi.org/10.1182/blood-2007-08-106583.

(85) Lu, L.; Lu, M.; Pei, Y.; Chen, J.; Qin, L.; Zhu, W.; Jia, H. Down-Regulation of SDF1-α Expression in Tumor Microenvironment Is Associated with Aspirin-Mediated Suppression of the pro-Metastasis Effect of Sorafenib in Hepatocellular Carcinoma. *Acta Biochim. Biophys. Sin. (Shanghai).* **2015**, *47* (12), 988–996. https://doi.org/10.1093/abbs/gmv112.

(86) Shaheen, R. M.; Davis, D. W.; Liu, W.; Zebrowski, B. K.; Wilson, M. R.; Bucana, C. D.; McConkey, D. J.; McMahon, G.; Ellis, L. M.; Machelon, V.; Emilie, D.; Terrassa, M.; Lackner, A.; Curiel, T. J.; Carmeliet, P.; Zou, W. Antiangiogenic Therapy Targeting the Tyrosine Kinase Receptor for Vascular Endothelial Growth Factor Receptor Inhibits the Growth of Colon Cancer Liver Metastasis and Induces Tumor and Endothelial Cell

Apoptosis. *Cancer Res.* **1999**, *59* (21), 5412–5416.

(87) Zeng, Y.; Li, B.; Liang, Y.; Reeves, P. M.; Qu, X.; Ran, C.; Liu, Q.; Callahan, M. V; Sluder, A. E.; Gelfand, J. A.; Chen, H.; Poznansky, M. C.; Zeng, Y.-; Li, B.; Liang, Y.; Reeves, P. M.; Qu, X.; Liu, Q.; Callahan, M. V; Sluder, A. E.; Chen, J. A. Dual Blockade of CXCL12-CXCR4 and PD-1-PD-L1 Pathways Prolongs Survival of Ovarian Tumor-Bearing Mice by Prevention of Immunosuppression in the Tumor Microenvironment. *FASEB J.* **2019**. https://doi.org/10.1096/fj.201802067RR.

(88) Van Goethem, E.; Poincloux, R.; Gauffre, F.; Maridonneau-Parini, I.; Le Cabec, V. Matrix Architecture Dictates Three-Dimensional Migration Modes of Human Macrophages: Differential Involvement of Proteases and Podosome-Like Structures. *J. Immunol.* **2010**, *184* (2), 1049–1061. https://doi.org/10.4049/jimmunol.0902223.

(89) Lämmermann, T.; Bader, B. L.; Monkley, S. J.; Worbs, T.; Wedlich-Söldner, R.; Hirsch, K.; Keller, M.; Förster, R.; Critchley, D. R.; Fässler, R.; Sixt, M. Rapid Leukocyte Migration by Integrin-Independent Flowing and Squeezing. *Nature* **2008**, *453* (7191), 51–55. https://doi.org/10.1038/nature06887.

(90) Janssen, L. M. E.; Ramsay, E. E.; Logsdon, C. D.; Overwijk, W. W. The Immune System in Cancer Metastasis: Friend or Foe? *J. Immunother. Cancer* **2017**, *5* (1), 79. https://doi.org/10.1186/s40425-017-0283-9.

(91) Parcesepe, P.; Giordano, G.; Laudanna, C.; Febbraro, A.; Pancione, M. Cancer-Associated Immune Resistance and Evasion of Immune Surveillance in Colorectal Cancer. *Gastroenterol. Res. Pract.* **2016**, *2016*, 1–8. https://doi.org/10.1155/2016/6261721.

(92) Cascone, R.; Carlucci, A.; Pierdiluca, M.; Santini, M.; Fiorelli, A. Prognostic Value of Soluble Major Histocompatibility Complex Class I Polypeptide-Related Sequence A in

Non-Small-Cell Lung Cancer – Significance and Development. *Lung Cancer Targets Ther.* **2017**, *Volume 8*, 161–167. https://doi.org/10.2147/LCTT.S105623.

(93) Textor, S.; Fiegler, N.; Arnold, A.; Porgador, A.; Hofmann, T. G.; Cerwenka, A. Human NK Cells Are Alerted to Induction of P53 in Cancer Cells by Upregulation of the NKG2D Ligands ULBP1 and ULBP2. *Cancer Res.* **2011**, *71* (18), 5998–6009. https://doi.org/10.1158/0008-5472.CAN-10-3211.

(94) Groh, V.; Wu, J.; Yee, C.; Spies, T. Tumour-Derived Soluble MIC Ligands Impair Expression of NKG2D and T-Cell Activation. *Nature* **2002**, *419* (6908), 734–738. https://doi.org/10.1038/nature01112.

(95) Weil, S.; Memmer, S.; Lechner, A.; Huppert, V.; Giannattasio, A.; Becker, T.; Müller-Runte, A.; Lampe, K.; Beutner, D.; Quaas, A.; Schubert, R.; Herrmann, E.; Steinle, A.; Koehl, U.; Walter, L.; von Bergwelt-Baildon, M. S.; Koch, J. Natural Killer Group 2D Ligand Depletion Reconstitutes Natural Killer Cell Immunosurveillance of Head and Neck Squamous Cell Carcinoma. *Front. Immunol.* **2017**, *8*, 387. https://doi.org/10.3389/fimmu.2017.00387.

(96) Barrera, L.; Montes-Servín, E.; Barrera, A.; Ramírez-Tirado, L. A.; Salinas-Parra, F.; Bañales-Méndez, J. L.; Sandoval-Ríos, M.; Arrieta, Ó. Cytokine Profile Determined by Data-Mining Analysis Set into Clusters of Non-Small-Cell Lung Cancer Patients According to Prognosis. *Ann. Oncol.* **2015**, *26* (2), 428–435. https://doi.org/10.1093/annonc/mdu549.

(97) Lee, S. O.; Yang, X.; Duan, S.; Tsai, Y.; Strojny, L. R.; Keng, P.; Chen, Y. IL-6 Promotes Growth and Epithelial-Mesenchymal Transition of CD133+ Cells of Non-Small Cell Lung Cancer. *Oncotarget* **2016**, *7* (6), 6626–6638. https://doi.org/10.18632/oncotarget.6570.

(98) Huang, A.-L.; Liu, S.-G.; Qi, W.-J.; Zhao, Y.-F.; Li, Y.-M.; Lei, B.; Sheng, W.-J.; Shen, H. TGF-B1 Protein Expression in Non-Small Cell Lung Cancers Is Correlated with Prognosis. *Asian Pac. J. Cancer Prev.* **2014**, *15* (19), 8143–8147.

(99) Ikushima, H.; Miyazono, K. TGFβ Signalling: A Complex Web in Cancer Progression. *Nat. Rev. Cancer* **2010**, *10* (6), 415–424. https://doi.org/10.1038/nrc2853.

(100) Nakasone, Y.; Fujimoto, M.; Matsushita, T.; Hamaguchi, Y.; Le Huu, D.; Yanaba, M.; Sato, S.; Takehara, K.; Hasegawa, M. Tumorigenesis and Neoplastic Progression Host-Derived MCP-1 and MIP-1 Regulate Protective Anti-Tumor Immunity to Localized and Metastatic B16 Melanoma. *Am J Pathol* **2012**, *180*, 365–374. https://doi.org/10.1016/j.ajpath.2011.09.005.

(101) Zhou, B.; Xu, H.; Ni, K.; Ni, X.; Shen, J. Expression of Chemokine XCL2 and CX3CL1 in Lung Cancer. *Med. Sci. Monit.* **2016**, *22*, 1560–1565. https://doi.org/10.12659/MSM.895985.

(102) Su, Y.-C.; Chang, H.; Sun, S.-J.; Liao, C.-Y.; Wang, L.-Y.; Ko, J.-L.; Chang, J. T. Differential Impact of CX3CL1 on Lung Cancer Prognosis in Smokers and Non-Smokers. *Mol. Carcinog.* **2018**. https://doi.org/10.1002/mc.22787.

(103) Gkretsi, V.; Stylianopoulos, T. Cell Adhesion and Matrix Stiffness: Coordinating Cancer Cell Invasion and Metastasis. *Front. Oncol.* **2018**, *8*, 145. https://doi.org/10.3389/fonc.2018.00145.

(104) Naba, A.; Clauser, K. R.; Lamar, J. M.; Carr, S. A.; Hynes, R. O. Extracellular Matrix Signatures of Human Mammary Carcinoma Identify Novel Metastasis Promoters. *Elife* **2014**, *3*. https://doi.org/10.7554/eLife.01308.

(105) Otegbeye, F.; Ojo, E.; Moreton, S.; Mackowski, N.; Lee, D. A.; Lima, M. de; Wald, D. N.

Inhibiting TGF-Beta Signaling Preserves the Function of Highly Activated, in Vitro Expanded Natural Killer Cells in AML and Colon Cancer Models. *PLoS One* **2018**, *13* (1), e0191358. https://doi.org/10.1371/JOURNAL.PONE.0191358.

(106) Nam, J.-S.; Terabe, M.; Mamura, M.; Kang, M.-J.; Chae, H.; Stuelten, C.; Kohn, E.; Tang, B.; Sabzevari, H.; Anver, M. R.; Lawrence, S.; Danielpour, D.; Lonning, S.; Berzofsky, J. A.; Wakefield, L. M. An Anti-Transforming Growth Factor Beta Antibody Suppresses Metastasis via Cooperative Effects on Multiple Cell Compartments. *Cancer Res.* **2008**, *68* (10), 3835–3843. https://doi.org/10.1158/0008-5472.CAN-08-0215.

(107) Ehrbar, M.; Sala, A.; Lienemann, P.; Ranga, A.; Mosiewicz, K.; Bittermann, A.; Rizzi, S. C.; Weber, F. E.; Lutolf, M. P. Elucidating the Role of Matrix Stiffness in 3D Cell Migration and Remodeling. *Biophys. J.* **2011**, *100* (2), 284–293. https://doi.org/10.1016/j.bpj.2010.11.082.

(108) Bruno, A.; Bassani, B.; D'Urso, D. G.; Pitaku, I.; Cassinotti, E.; Pelosi, G.; Boni, L.; Dominioni, L.; Noonan, D. M.; Mortara, L.; Albini, A. Angiogenin and the MMP9–TIMP2 Axis Are up-Regulated in Proangiogenic, Decidual NK-like Cells from Patients with Colorectal Cancer. *FASEB J.* **2018**, *32* (10), 5365–5377. https://doi.org/10.1096/fj.201701103R.

(109) Ishida, Y.; Migita, K.; Izumi, Y.; Nakao, K.; Ida, H.; Kawakami, A.; Abiru, S.; Ishibashi, H.; Eguchi, K.; Ishii, N. The Role of IL-18 in the Modulation of Matrix Metalloproteinases and Migration of Human Natural Killer (NK) Cells. *FEBS Lett.* **2004**, *569* (1–3), 156–160. https://doi.org/10.1016/j.febslet.2004.05.039.

(110) Yang, B.; Liu, H.; Shi, W.; Wang, Z.; Sun, S.; Zhang, G.; Hu, Y.; Liu, T.; Jiao, S. Blocking Transforming Growth Factor-β Signaling Pathway Augments Antitumor Effect

of Adoptive NK-92 Cell Therapy. *Int. Immunopharmacol.* **2013**, *17* (2), 198–204. https://doi.org/10.1016/J.INTIMP.2013.06.003.

(111) Ikeda, H.; Old, L. J.; Schreiber, R. D. The Roles of IFNγ in Protection against Tumor Development and Cancer Immunoediting. *Cytokine Growth Factor Rev.* **2002**, *13* (2), 95–109. https://doi.org/10.1016/S1359-6101(01)00038-7.

(112) Roda, J. M.; Parihar, R.; Magro, C.; Nuovo, G. J.; Tridandapani, S.; Carson, W. E. Natural Killer Cells Produce T Cell-Recruiting Chemokines in Response to Antibody-Coated Tumor Cells. *Cancer Res.* **2006**, *66* (1), 517–526. https://doi.org/10.1158/0008-5472.CAN-05-2429.

(113) Dorner, B. G.; Smith, H. R. C.; French, A. R.; Kim, S.; Poursine-Laurent, J.; Beckman, D. L.; Pingel, J. T.; Kroczek, R. A.; Yokoyama, W. M. Coordinate Expression of Cytokines and Chemokines by NK Cells during Murine Cytomegalovirus Infection. *J. Immunol.* **2004**, *172* (5), 3119–3131. https://doi.org/10.4049/jimmunol.172.5.3119.

(114) Fauriat, C.; Long, E. O.; Ljunggren, H.-G.; Bryceson, Y. T. Regulation of Human NK-Cell Cytokine and Chemokine Production by Target Cell Recognition. *Blood* **2010**, *115* (11), 2167–2176. https://doi.org/10.1182/blood-2009-08-238469.

(115) Menten, P.; Wuyts, A.; Van Damme, J. Macrophage Inflammatory Protein-1. *Cytokine Growth Factor Rev.* **2002**, *13* (6), 455–481. https://doi.org/10.1016/S1359-6101(02)00045-X.

(116) Wen, F. T.; Thisted, R. A.; Rowley, D. A.; Schreiber, H. A Systematic Analysis of Experimental Immunotherapies on Tumors Differing in Size and Duration of Growth. *Oncoimmunology* **2012**, *1* (2), 172–178.

(117) Gulley, J. L.; Madan, R. A.; Schlom, J. Impact of Tumour Volume on the Potential

Efficacy of Therapeutic Vaccines. *Curr. Oncol.* **2011**, *18* (3), e150-7.

Table of Contents Graphic

Engineered Three-Dimensional Tumor Models to Study Natural Killer Cell Suppression

Madison N. Temples, Isaac M. Adjei, Phoebe M. Nimocks, Julie Djeu, Sheng Wei, and Blanka Sharma

***For Table of Contents Use Only**